# Lawrence Berkeley National Laboratory

Title

A critical dislocation velocity for serration mechanism transition in a nickel–chromium
solid solution alloy

Permalink

Authors

Qin, Yu
Greaney, P Alex
Evans, T Matthew
et al.

Publication Date

DOI

Copyright Information

Peer reviewed

# A Critical Dislocation Velocity for Serration Mechanism Transition in a Nickel-Chromium Solid Solution Alloy

Qin Yu[a,1], P. Alex Greaney[b,2], T. Matthew Evans[c], Jamie J. Kruzic[d,3]

[a] *School of Mechanical, Industrial, & Manufacturing Engineering, Oregon State University, Corvallis, OR 97331, USA*

[b] *Mechanical Engineering Department, University of California — Riverside, Riverside, CA 92501, USA*

[c] *School of Civil & Construction Engineering, Oregon State University, Corvallis, OR 97331, USA*

[d] *School of Mechanical and Manufacturing Engineering, University of New South Wales (UNSW Sydney), Sydney NSW 2052, Australia*

**Abstract:** The influence of strain rate across three orders of magnitude ($1.70 \times 10^{-5}$ /s to $1.43 \times 10^{-2}$ /s) along with the effect of the plastic strain accumulation (up to 10%) on the serrated plastic flow were investigated in the nickel-chromium (Ni-Cr) solid solution alloy Nimonic 75 by performing constant-strain-rate tension testing at 600 °C. As the strain rate decreased, the critical strain for the onset of serrations transitioned from normal behavior to inverse behavior. The serrated flow was characterized as Type A+B serration at high strain rate ($1.43 \times 10^{-2}$ /s). In the intermediate strain-rate regime ($1.43 \times 10^{-3}$ /s and $1.45 \times 10^{-4}$ /s), Type B serrations were observed and followed by a transformation to Type C+B serrations. At the low strain rate ($1.70 \times 10^{-5}$ /s), the plastic flow immediately displayed Type C serrations, which later evolved into Type C+B serrations. Regardless of the strain rate, plastic strain, or dislocation density, a critical dislocation velocity falling in the range of $1.2 \times 10^{-6} - 2.2 \times 10^{-6}$ m/s was identified to signify the onset of Type C (or C+B) serration, whereby the mobile dislocations break free from the solute cloud for short bursts of deformation. Finally, a novel model by solute rearrangement across dislocation cores was used to understand how the critical dislocation velocity is quantitatively determined by the rate at which solute atoms are able to hop across the glide plane as a partial dislocation core moves through the lattice.

---

[1] Present address: Materials Sciences Division, Lawrence Berkeley National Laboratory, Berkeley, CA 94720, USA
[2] Corresponding author: agreaney@engr.ucr.edu
[3] Corresponding author. j.kruzic@unsw.edu.au

## 1. Introduction

### 1.1. Background

One concern for high-temperature deformation of metallic alloys is inhomogeneous plastic deformation (or plastic instability). This phenomenon is associated with discontinuous yielding or serrated plastic flow, which is generally referred to as the Portevin–Le Chatelier (PLC) effect (Rodriguez, 1984; Yilmaz, 2011; Zhang et al., 2017). The macroscopic response involves alternating stress rises and drops that are successively observed in the stress-strain curves when testing conditions fall within certain regimes of temperature and strain rate. Serrated flow has been observed in a wide range of interstitial/solid solution alloys, such as Al-Mg alloys (Fu et al., 2012; Picu et al., 2005; Robinson, 1994; Yuzbekova et al., 2017), Fe-based alloys (Bian et al., 2017; Cuddy and Leslie, 1972; Hall, 1970; Hong and Lee, 2005; Lan and Zhang, 2017; Zhang and Jiang, 2005), Ni-based superalloys (Gopinath et al., 2009; G.-M. Han et al., 2015; G. M. Han et al., 2015; Shankar et al., 2017), Mg alloys (Li et al., 2011; Wang et al., 2017; Zhu and Nie, 2004), and high entropy alloys (Carroll et al., 2015; Komarasamy et al., 2017; Tsai et al., 2019). Typical serration phenomena have been extensively documented in several review articles (Rodriguez, 1984; Yilmaz, 2011; Zhang et al., 2017).

The micro-mechanism responsible for the onset of serrated flow is associated with the interaction between mobile dislocations and the diffusing solute atmosphere, which is known as dynamic strain aging (DSA). An early model proposed by Cottrell and Bilby (1949) considered that the mobility of solute atoms is sufficiently high to allow solute atoms to diffuse through the lattice and follow the movement of gliding dislocations. When the average dislocation velocity is sufficiently slow, there is sufficient time for the solute field to segregate to dislocations and to relax the evolving dislocation strain field, dissipating energy and creating viscous drag that hinders dislocation motion. As the dislocation velocity is increased, or as the friction stress exerted by the solute cloud is exceeded, dislocations can "break away" from the solute cloud and move more freely. This theory is thought to work well for low-strain-rate deformation at high temperature. However, in cases of high-strain-rate deformation and low temperature, the solute

diffusion rate is generally lower than the velocity of dislocations. To account for this, Sleeswyk (1958) and McCormigk (1972) modified Cottrell's model by assuming that solute atoms will diffuse to mobile dislocations during temporary arrests at obstacles (*e.g.*, forest dislocations, precipitates, *etc.*) in their glide paths. If the stress rises more slowly than the pinning strength imbued by the solute, dislocations will become continually repined by solute after every slip event. The plastic strain at which the average dislocation arrest time ("waiting time") is equal to the time required to lock the arrested dislocation ("aging time") is defined as a *critical strain* to indicate the onset of serrated flow. Under conditions of high-strain-rate deformation and low temperature, the critical strain increases with increasing strain rate and decreasing temperature, which is regularly referred to as the "normal behavior." In parallel, there exists an "inverse behavior," usually occurring under the conditions of slow strain rate and high temperature, where the critical strain decreases with increasing strain rate and decreasing temperature. It is noted that McCormick's model (McCormigk (1972)) fails to rationalize the inverse behavior of critical strain. To fill in this gap, Fu et al. (2012) proposed a model which attributes the occurrence of serration in regimes of slow strain rate and high temperature to the unpinning process, where the pinned dislocations escape from the locking solute cluster. Their unpinning-dominant model is able to account for the inverse behavior of critical strain. Along with the development of phenomenological model for DSA mechanism, Curtin et al., 2006 proposed a cross-core diffusion mechanism, pointing out that the DSA mechanism is ascribed to a single-atomic jump of solutes across the slip plane from the compression to the tension side of dislocation core. Their cross-core model made accurate prediction of strength and strain rate in application to aluminum-magnesium alloys.

Following the onset of serration, various serration shapes will be present on the stress-strain curves. Serrated flow is commonly classified into four groups, namely: Type A, Type B, Type C, and Type D (Rodriguez, 1984; Yilmaz, 2011; Zhang et al., 2017). The difference between serration types lies in their varied behaviors of stress rise and stress drop with respect to the general stress level or locus, which can be simply regarded as the smooth stress-strain curve prior to the onset of serration. For Type A serration, the plastic flow shows an abrupt stress rise followed by a stress drop that will bring the stress back to, or below, the general level of the stress-strain curve. Microscopically, repeated deformation bands are initiated at one end of specimen and propagate smoothly in one direction. Type A serrations are commonly observed

under relatively high strain rates and at relatively low temperatures, where the stress rise is attributed to the locking of mobile dislocations. Type B serrations appear as oscillations above and below the general level of the stress-strain curve and microscopically discontinuous deformation band propagation is observed. Type B serrations often follow after each Type A stress drop, forming a Type A+B serration classification. Alternatively, Type B serrations are observed to occur alone at the onset of serrated yielding at intermediate temperature and strain rates. Type C serrations manifest as sudden stress drops below the general level of the stress-strain curve. Afterwards, the stress gradually returns to the general level of the flow curve. The stress drop is attributed to the dislocation unlocking process. Finally, Type D serration is generally referred to sequential stress plateaus with zero work-hardening rate often formed in a "stair-stepping" pattern in the stress-strain curve. The stress plateau is usually associated with propagation of Lüders bands in the gage section.

*1.2. Motivation and objectives*

In investigations of serration behavior for interstitial and substitutional solid solution alloys, most commonly a single serration type was exhibited under constant strain-rate loading at a specified temperature. Very limited literature has addressed the transformation of serration type with respect to an accumulation of plastic strain (Ozgowicz and Grzegorczyk, 2008; Rodriguez, 1984). As one example, transitions from serrations of Type A, through Type A+B, and to Type B were observed for a tin-bronze alloy deformed at $1.2 \times 10^{-3}$ /s at 150 °C (Ozgowicz and Grzegorczyk, 2008). The lack of literature might be partially due to the insufficient accuracy in measuring the engineering strain without using a high-resolution strain gauged extensometer at elevated temperatures. Because of the limited investigations into the serration-type transformation, studies regarding the associated DSA mechanisms are also limited. Motivated by the limited mechanistic understanding of serration mechanism transitions, the present study focuses on the investigation of serration transitions as a function of both the strain rate and the accumulated plastic strain.

The material selected is one of the simplest commercially available nickel-chromium solid solution alloys, Nimonic 75. This nickel superalloy was first introduced in 1940s to fabricate turbine blades in Whittle jet engines (Betteridge and Heslop, 1974; Reed, 2006). More recently, Nimonic 75 has been certified as a reference material for ambient-temperature tensile testing

(Ingelbrecht and Loveday, 2000; Vandermeulen et al., 2017) and high-temperature creep testing (Gould and Loveday, 1990). The motivations for the selection of Nimonic 75 alloy are twofold: (1) the deformation mechanisms (including DSA mechanism) in Nimonic 75 alloy should be relatively simpler to uncover than more heavily alloyed solid solution and precipitation hardening superalloys based on Ni-20Cr. (2) This is a certified reference alloy used as the qualification of testing data; accordingly, a highly controlled microstructure can be readily purchased for mechanistic studies that can be repeated in laboratories around the world. The deformation mechanisms revealed by this study are expected to be valuable for developing and validating advanced mechanism-informed deformation, creep, and failure models, as suggested in Truszkowska et al. (2017). Accordingly, the scope of the present study is to investigate the serrated plastic flow behavior for Nimonic 75 with the goal of developing a mechanistic understanding of how serration types transition as a function of strain rate and strain accumulation, and the solute drag mechanism that underpins them.

## 2. Material and experiment

### 2.1. Material

Nickel-chromium alloy Nimonic 75 (Betteridge and Heslop, 1974) was selected as the material for this study. While this alloy is certified as a tensile and creep reference material (Gould and Loveday, 1990; Ingelbrecht and Loveday, 2000; Vandermeulen et al., 2017), open literature on the elevated-temperature deformation (Betteridge and Heslop, 1974; Guo et al., 2007; Ward and Tallis, 1956) and creep deformation (Hayes et al., 2017) is limited, with negligible information available on the serrated flow behavior. Certified rods were acquired from LGC Standards (Teddington, Middlesex, United Kingdom). The nominal chemical composition of Nimonic 75 is summarized in Table 1.

**Table 1** Nominal chemical composition of Nimonic 75 alloy in wt%.

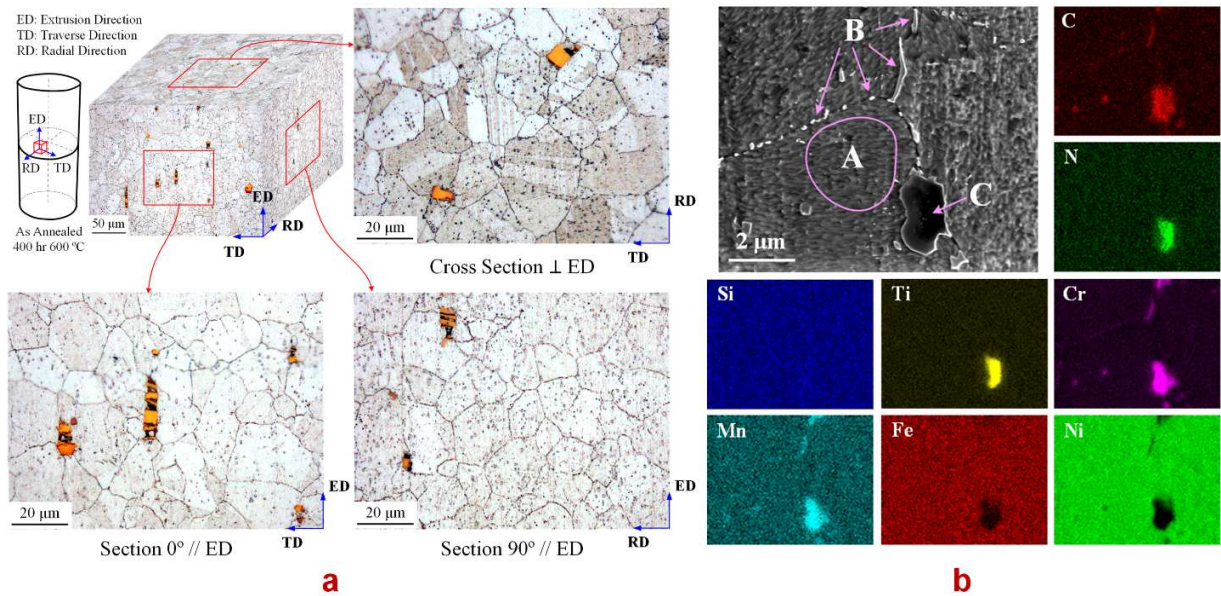| Ni | Cr | Ti | C | Si | Cu | Fe | Mn |
|---------|-----------|---------|-----------|---------|---------|---------|---------|
| Balance | 18.0-21.0 | 0.2-0.6 | 0.08-0.15 | 1.0 max | 0.5 max | 5.0 max | 1.0 max |

**Fig. 1.** Microstructure of the annealed Nimonic 75 alloy before the mechanical experiment. (a) Three-dimensional stereography of the optical microstructure reveals an equiaxed grain structure with an average grain size of 18 µm. (b) Three phases were identified by SEM/EDS mapping: (1) gamma matrix phase (Circle A), (2) inter- & intra-granular CrMn-rich carbides (Arrows B), and (3) individual large polyhedron-shaped TiCrMn-rich carbonitrides (Arrow C).

The as-received material was annealed at 600 °C for 400 h and furnace cooled to form stable carbides at the grain boundaries that are typical for this class of superalloys. The annealed microstructure was examined on three orthotropic planes which are perpendicular to the extrusion direction (ED), the traverse direction (TD), and the radial direction (RD), respectively (Fig. 1a). In order to reveal the grain structure and the phases, the sample surfaces were ground using SiC paper up to 800 grit and polished using polycrystalline diamond suspension with particle sizes of 6 µm and 1 µm. Final polishing was achieved using an alumina suspension with particle size of 0.05 µm. The polished sample surface was etched by Fry's reagent composed of 150 mL water, 50 mL HCL, 25 mL HNO$_3$, and 1g CuCl$_2$. The three-dimensional stereography of the optical microstructure for the annealed Nimonic 75 alloy (Fig. 1a) reveals an equiaxed grain structure with an average grain size of 18 µm. The grain size was measured using the mean lineal intercept method without counting the twin boundaries. Energy dispersive X-ray spectroscopy (EDS) mapping disclosed the existence of three phases in the annealed material (Fig. 1b): (1) gamma matrix phase (Circle A, Fig. 1b), (2) inter- & intra-granular CrMn-rich carbides (Arrows

6

B, Fig. 1b), and (3) individual large polyhedron-shaped TiCrMn-rich carbonitrides (Arrow C, Fig. 1b).

## 2.2. Tensile experiments

Dog-bone cylinder-shaped testing specimens with a gauge length of 25 mm were used for elevated temperature tensile experiments in accordance with ASTM E8 and E21 standards (ASTM International, 2009; ASTM International, 2009a). The geometry and dimensions of the tensile testing specimen are specified in Fig. 2a. The gauge section and the grip section of the high-temperature testing specimen were designed to be long enough to allow for induction heating via a copper coil (Fig. 2b). Three K-type thermocouples were attached to the specimen surface by spot welding within the gauge section at the midpoint, 12.5 mm above the midpoint, and 12.5 mm below the midpoint (Fig. 2c). The midpoint thermocouple was used to control the target temperature, whereas, the two 12.5 mm-away thermocouples were used to monitor the uniformity of the temperature distribution within the gauge section (Fig. 2d).
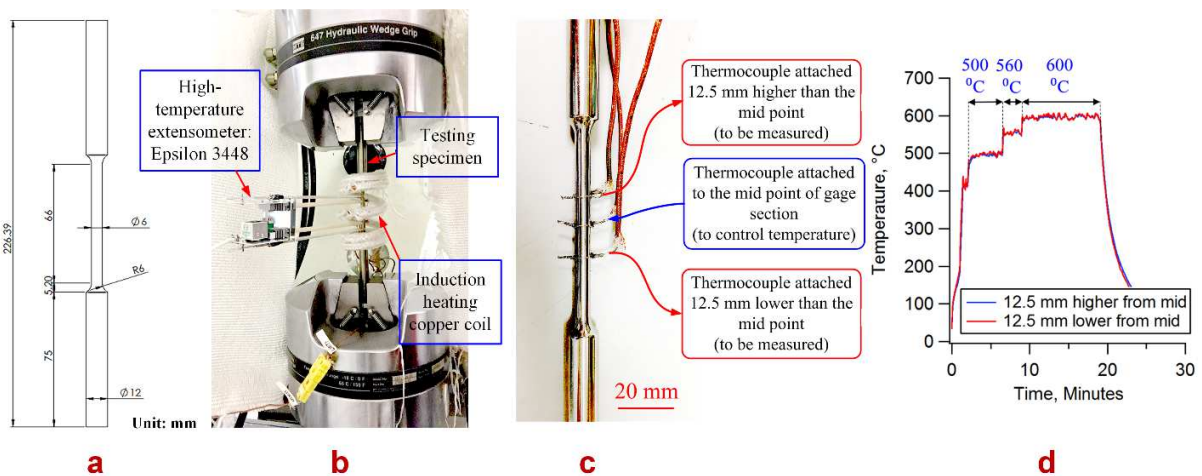


**Fig. 2.** (a) Geometry and dimensions of the tensile dog-bone specimen. (b) Experimental setup for elevated-temperature tension experiments. The induction heating coil was used to heat the specimen whereas the high-temperature extensometer was used to measure the strain. (c) Locations within the gauge section where the K-type thermocouples were spot welded. (d) Uniform temperature distribution was verified within the gauge section before and during the mechanical testing.

Uniaxial tension experiments were performed using a computer controlled, 250 kN capacity servohydraulic load frame (Model 810, MTS Systems Corporation, Eden Prairie, MN, USA) in displacement control at four constant speeds: 0.001 mm/s, 0.01 mm/s, 0.1 mm/s, and 1 mm/s. Load was measured using a calibrated 25 kN capacity load cell. A high-temperature extensometer (Model 3448, Epsilon Technology Corporation, Jackson, WY, USA) with a gauge length of 25 mm was mounted to the specimen surface to measure the engineering strain (Fig. 2b). Before applying the mechanical loading, the specimen was heated up to 600 °C by induction-heating using a copper coil. A uniform temperature distribution along the gauge section was ensured by tracking temperatures acquired from the upper and lower thermocouples welded at the ends of the gauge section (Fig. 2d). Each specimen was monotonically tensioned up to a strain of 10% and unloaded. Because the extensometer arms opened up during the elongation of the specimen, the tensile strain was limited to 10% to prevent the contact of the extensometer arms with the induction-heating coil. After the experiment was completed, the actual strain rate was calculated from the true strain derived from the measured engineering strain. The actual strain rates corresponding to the four controlled displacement rates were $1.70\times10^{-5}$ /s, $1.45\times10^{-4}$ /s, $1.43\times10^{-3}$ /s, and $1.43\times10^{-2}$ /s, respectively, all of which fall in the range of quasi-static strain rates. Strain rates higher than this are beyond the capabilities of our current experimental setup. For each strain rate, two tests were conducted to evaluate the repeatability. True stress and true strain were calculated and reported.

## 3. Results

Representative true stress-strain curves for Nimonic 75 alloy tensioned under the four strain rates at 600 °C are shown in Fig. 3a. For better visualization, the stress-strain curves are shifted along the strain axis using a strain interval, $\Delta$, of 0.015. To evaluate the elastic properties of the material, the Young's modulus and the elastic proportional limit were extracted from the tensile stress-strain curves (Fig. 3b and c) by determining the best fit linear region of the elastic data (refer to Appendix A for more details). As shown in Fig. 3b, the strain rates within the investigated range have insignificant effect on the elastic properties. The determined average Young's modulus and the average elastic proportional limit were 168 GPa and 211 MPa, respectively. The 0.2 % offset yield strength is plotted with respect to the strain rate in Fig. 3c. A trend of decreasing yield strength with increasing strain rate is observed. This "inverse yield

stress" or "negative strain-rate sensitivity (nSRS)" behavior indicates that the alloy is undergoing dynamic strain aging (Rodriguez, 1984). A detailed investigation into the serrated plastic flow will be presented in the following sections.
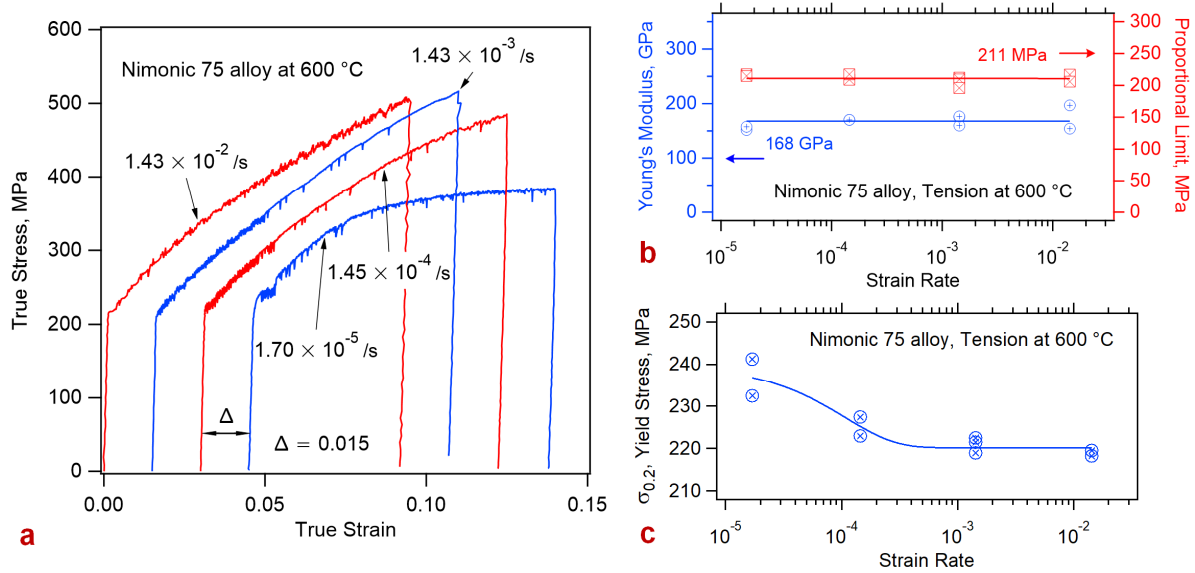


**Fig. 3.** (a) True stress-strain curves for Nimonic 75 alloy tensioned under four constant strain rates from $1.70 \times 10^{-5}$ /s to $1.43 \times 10^{-2}$ /s at 600 °C. (b) Variations of the Young's modulus and the elastic proportional limit with respect to the strain rate. (c) Variation of the 0.2 % offset yield stress with respect to the strain rate.

## 4. Discussion

### 4.1. Serrated flow and identification of serration types

Clearly observed from the stress-strain curves (Fig. 3a) and as inferred by the inverse yield stress behavior (Fig. 3c), serrated flow occurs in Nimonic 75 alloy at all the investigated strain rates. Fig. 4 displays the serration characteristics in more detail. Note that in Fig. 4, the true plastic strain was obtained by subtracting the elastic strain from the total strain using the Young's modulus determined in Fig. 3b. In the following discussion, the serration types and their transition will be examined by inspecting the characteristic behavior of stress rise and stress drop in the stress-plastic strain curves piecewise with respect to the accumulation of plastic strain, from the onset of yielding to the latter plastic deformation, for the four controlled strain rates. The reliability of the identification of the serration transition by direction observation was verified using a numerical algorithm, the details of which can be found in Appendix C.
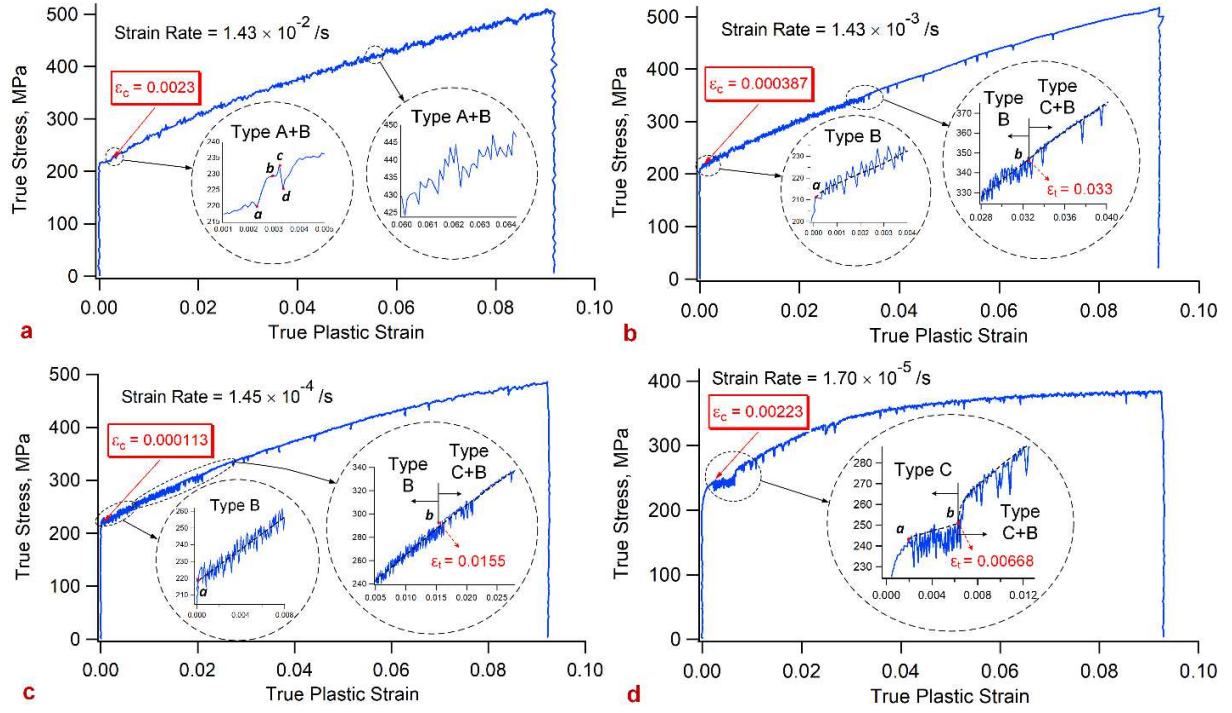
**Fig. 4.** Representative true stress-plastic strain curves with the corresponding serration types at each of the four strain rates: (a) $1.43\times10^{-2}$ /s; (b) $1.43\times10^{-3}$ /s; (c) $1.45\times10^{-4}$ /s; (d) $1.70\times10^{-5}$ /s.

At the highest strain rate of $1.43\times10^{-2}$ /s (Fig. 4a), the material macroscopically yielded at a stress of 216 MPa. Afterwards, stable plastic flow occurred with a low strain-hardening rate ($\Delta\sigma/\Delta\varepsilon_p \approx 1477$ MPa) until an abrupt stress rise was detected at a plastic strain of 0.0023 (point *a* in Fig. 4a). The stress rise was composed of two stages. During the first stage, the stress increased rapidly ($\Delta\sigma \approx 9.4$ MPa) until a yielding point *b* was reached. A second stress rise increment ($\Delta\sigma \approx 3.1$ MPa) followed until a peak stress (point *c* in Fig. 4a) was reached. Although the second-stage stress rise was smaller than that in the first stage, the strain hardening rate in the second stage was somewhat higher with $\Delta\sigma/\Delta\varepsilon_p \approx 17075$ MPa for the first stage and $\Delta\sigma/\Delta\varepsilon_p \approx$ 20242 MPa for the second stage. The two-stage stress rise reflects an aging effect caused by the solute diffusing to the mobile dislocations. This solute aging effect reached a maximum degree at the peak point *c* (Fig. 4a), where the mobile dislocations reached a maximum pinning stress induced by the solute clouds (Rodriguez, 1984). Immediately after the peak stress, the stress dropped rapidly back to the general level of the stress-plastic strain curve. This stress drop is associated with the release of the pinned dislocations. The stress rise-drop described above is a typical Type-A serration. Moreover, small stress oscillations accompanied the Type-A stress

10

rises and drops from the beginning of the observed serrated flow. This secondary Type-B stress oscillation accompanying the primary Type-A serrations became more obvious with increasing strain (Fig. 4a). Therefore, the serration type for this strain rate was designated as Type A+B.

As the strain rate was lowered to $1.43\times10^{-3}$ /s, the onset of serrated flow was detected as a stress drop immediately after the material yielded at a plastic strain of 0.000387 (point *a* in Fig. 4b). Sequences of stress rises and drops were followed successively, appearing to oscillate about the general level of the stress-plastic strain curve. This is typical Type-B serration behavior. Such Type-B serration behavior terminated at a plastic strain of 0.033 (point *b* in Fig. 4b), where the stress-plastic strain curve exhibited an abrupt stress drop followed by a gradual stress rise, returning the stress back to the general level. Here the dominant serration type changed from Type B to Type C with considerable strain intervals between each sequential Type-C serration. Type-B stress oscillations in small magnitudes persisted between the Type-C "teeth," suggesting here Type C+B serrated flow occurs. At the next lower strain rate of $1.45\times10^{-4}$ /s, the serrated flow started with a stress rise occurring at a very small plastic strain of 0.000113 (point *a* in Fig. 4c). The subsequent stress rises and drops followed a Type-B behavior similar to that exhibited at the strain rate of $1.43\times10^{-3}$/s. At a plastic strain of 0.0155 (point *b* in Fig. 4c), the continuous Type-B serration terminated and a Type C+B serration was observed.

In contrast to the high and intermediate strain rates, for the slowest strain rate of $1.70\times10^{-5}$ /s, serrated flow began with Type C serrations, which later transformed to Type C+B (Fig. 4d). It is interesting to note that during the initial Type C serration stage, the general locus of the stress-plastic strain curve shows a relatively low strain hardening rate. Another distinctive feature of this strain rate is related to the transformation point of serration from Type C to Type C+B (point *b* in Fig. 4d). At the transformation point, the strain hardening rate of the general stress-strain locus increased abruptly. This is different from the transformation points at strain rates of $1.43\times10^{-3}$ /s and $1.45\times10^{-4}$ /s, where a continuity of strain hardening exists at the strain where Type B serration is transformed to Type C+B serration (compare Fig. 4b and c with Fig. 4d).

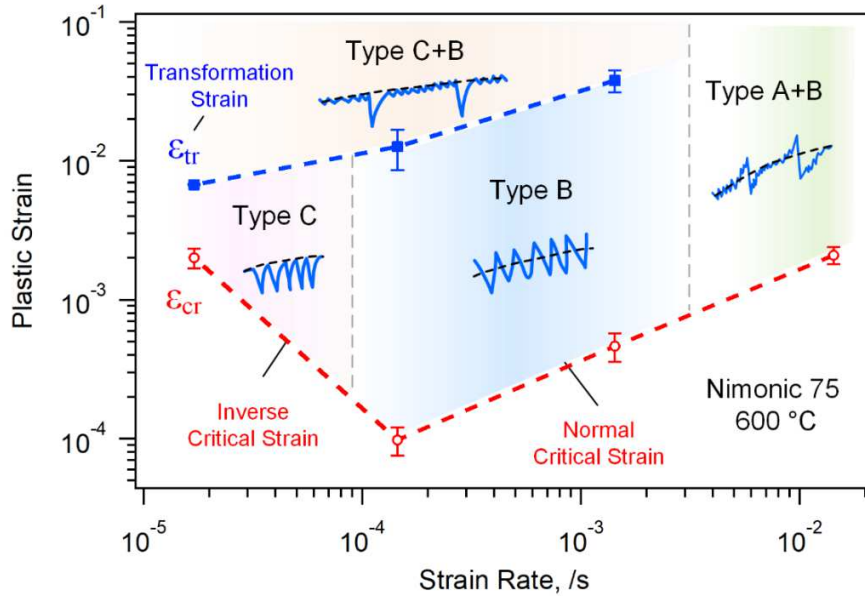*4.2. Serration map, critical strain, and transformation strain*

11

**Fig. 5.** Serration map showing the variation of serration types with respect to the applied strain rate and the accumulated plastic strain. The critical strain ($\varepsilon_{cr}$), which signifies the onset of serrated flow, and the transformation strain ($\varepsilon_{tr}$), which indicates the transition between serration types, are also indicated.

The serration behavior in Nimonic 75 at 600 °C is summarized in a serration map which is constructed as a function of the applied strain rate and the accumulated plastic strain (Fig. 5). Both the vertical plastic strain axis and the horizontal strain rate axis are plotted in logarithmic scale. The critical strain, $\varepsilon_{cr}$, which signifies the onset of serrated flow, and the transformation strain, $\varepsilon_{tr}$, which indicates the transition between serration types, are also displayed in Fig. 5. As the applied strain rate is increased from $1.70 \times 10^{-5}$ /s to $1.43 \times 10^{-2}$ /s, the critical strain changes from an inverse behavior to a normal behavior near the strain rate of $1.43 \times 10^{-4}$ /s. Correspondingly, the initial serrated flow behavior changes from Type C in the inverse critical strain regime, to Type B near the transition, and then to Type B and Type A+B in the normal critical strain regime. This observation of critical strain behavior is consistent with other findings in literature, *i.e.* that, the "normal critical strain" behavior is associated with Type A or B serration, whereas, the "inverse critical strain" behavior is related to Type C serration.

For the low and intermediate strain rates, it was found that pure Type C or Type B serration behavior is transformed into a Type C+B serration behavior when a sufficient amount of plastic strain is accumulated. As shown in Fig. 5, the transformation strain increases with increasing

strain rate. For most interstitial and substantial solid solution alloys, a single serration type was commonly observed under a specified condition of strain rate and temperature. Very limited literature has addressed the transformation of serration type with respect to the accumulation of plastic strain (Ozgowicz and Grzegorczyk, 2008; Rodriguez, 1984). As one example, a transformation from Type A, to Type A+B, and finally to Type B serrations was reported for a tin-bronze (CuSn7) alloy with an addition of 0.1%-Zr deformed at $1.2 \times 10^{-3}$ /s at 150 °C (Ozgowicz and Grzegorczyk, 2008). At the same strain rate but at 280 °C, a slightly different CuSn7 alloy with only 0.01%-Zr added demonstrated instead a transformation from Type B to Type C serration. This latter case is consistent with our current result where Type B to Type C+B was observed during plastic flow at the intermediate strain rates.

*4.3. The controlling mechanisms for various serration types*

As revealed in Fig. 5, with decreasing applied strain rate, the critical strain that signifies the onset of serrated flow first decreases and then increases. This corresponds initially to a normal behavior in the high-strain-rate regime but an inverse behavior in the low-strain-rate regime. Correspondingly, the serration type transforms from Type A+B, through Type B, and then to Type C as the applied strain rate is decreased. These features suggest the dynamic strain aging (DSA) mechanisms are distinct at different strain rates. In the context of the present experimental results, the various DSA mechanisms associated with Type A, Type B, and Type C serrations for Nimonic 75 alloy are discussed as follows.

Under relatively high-strain-rate and/or low-temperature conditions, Type A serration is generally found (Fig. 6a). The macroscopic stress-strain response in a typical Type A serration compromises two stages: (i) a two-stage stress rise above the general stress level with initially low and later high strain hardening rates (P2 to P3); (ii) a fast stress drop to the general level right after the local peak stress (P3 to P4). Since the applied strain rate is high, it is reasonable to assume the average velocity of mobile dislocations ($\bar{v}_m$) is higher than the average velocity of the solute atoms ($\bar{v}_S$), *i.e.* $\bar{v}_m > \bar{v}_S$, and thus between the serration events dislocations are gliding relatively free from the solute drag (such as P1 to P2). We refer to this as *low-drag motion*. During the gliding of mobile dislocations, solute atoms will segregate at the junctions of mobile dislocations and forest dislocations due to lattice diffusion and pipe diffusion as indicated by the solid red and dotted violet arrows in Fig. 6, respectively. The solute segregation forms the so-

called Cottrell-atmosphere (Cottrell and Bilby, 1949). The continued segregation process will increase the solute concentration of the Cottrell-atmosphere, hindering the movement of dislocations $((\bar{v}_m)_{P_3} < (\bar{v}_m)_{P_2})$ and thus causing an increase of the external stress to sustain deformation. During the stress rising (P2 to P3), the solute concentration will be intensified to a critical value and the dislocation velocity decreases. Correspondingly the stress rises to a local peak (P3 in Fig. 6a). The microscope processes from P2 to P3 is regularly terms as a "*pinning process.*" Beyond point P3, the friction stress exerted to the solute-locked dislocation is exceeded, and the pinned dislocations can "break away" from the solute clouds and move more freely, leading to a speedy stress drop and a restoration of the average dislocation velocity (P4 in Fig. 6a). Compared to the rapid *de-pinning process* (P3 to P4), a greater amount of strain/time is required during the solute segregation and pinning process (P2 to P3). In short, the rate limiting DSA mechanism which governs Type A serration behavior is driven by the pinning process, during which solute atoms diffuse and segregate towards the dislocation junctions.
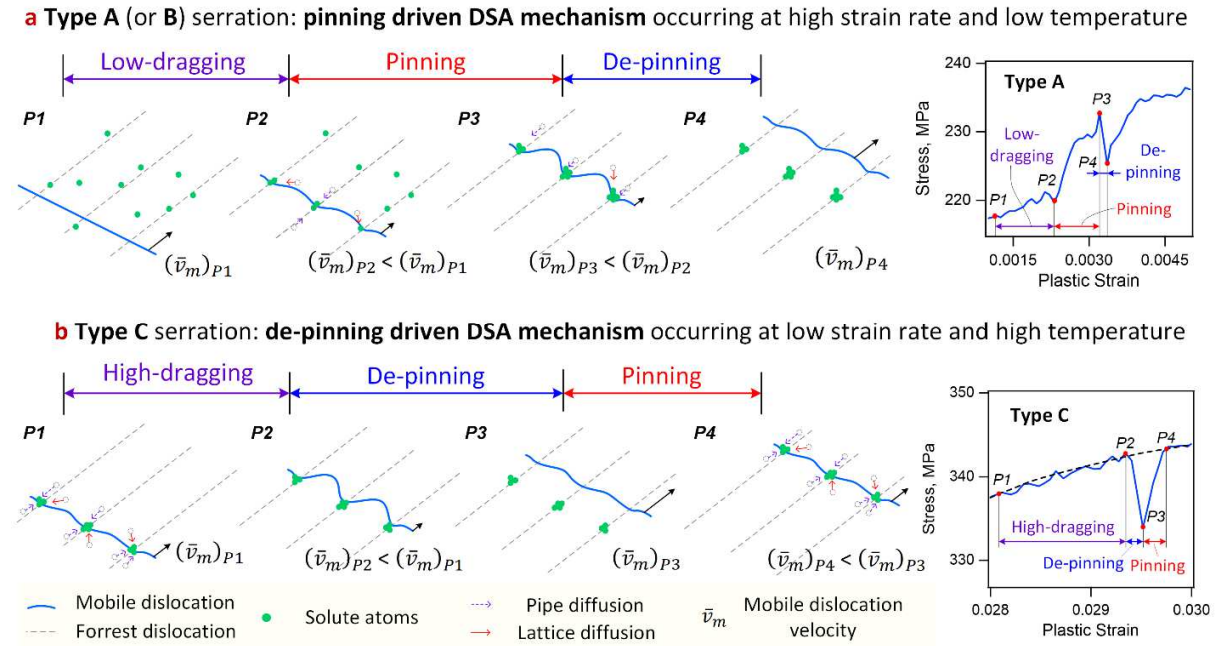


**Fig. 6.** Schematic diagrams illustrating the microscopic processes associated with dynamic strain aging (DSA) mechanisms underlying: (a) Type A (or B) serration driven by the pinning process occurring at relatively high strain rate and/or low temperature; (d) Type C serration driven by the de-pinning process taking place at relatively low strain rate and/or high temperature.

Although the stress response in Type B serration differs from that of Type A, the DSA mechanism of Type B serration is still driven by the pinning process shown in Fig. 6a. Due to the decreased strain rate in the loading case incurring Type B serration, the dislocation mobility is reduced. At a given temperature, where the diffusion rate is constant, the reduction of dislocation mobility shortens the time/strain span of the pinning process, making the strain/time expended in the pinning process (P2 to P3 in Fig. 6a) comparable to that of the de-pinning process (P3 to P4 in Fig. 6a). Thereby, the pinning process and the de-pinning process make almost equal contributions to Type B serrations, resulting in similar responses of the stress rises and drops.

Unlike Type A (or B) serration, Type C serration, which appears under conditions of relatively low strain rate and/or high temperature, is controlled microscopically by a DSA mechanism driven by the de-pinning process. Typical Type C serration is macroscopically characterized by a significant stress drop below the general level of the stress-strain curve followed by a stress rise that will gradually return the stress back to the general level (Fig. 6b). The slow strain rate is expected to reduce the average velocity of mobile dislocations ($\bar{v}_m$) to a value smaller than the average velocity of the solute atoms ($\bar{v}_S$), *i.e.*, $\bar{v}_m < \bar{v}_S$. During the stable plastic deformation between serrations, the solute atoms can easily diffuse and segregate to the dislocation junctions. A saturation of solute cloud concentration will be quickly reached during the development of stable plastic strain, *e.g.*, at P1 in Fig. 6b. As the plastic deformation is continued, the mobile dislocations glide and drag the saturated solute cloud. In Fig. 6b we refer to this as *high-drag motion*. Due to the dragging effect induced by the solute cloud, the average velocity of the mobile dislocations is reduced, resulting in an increase of the external stress. At P2 (Fig. 6b), the critical stress for breaking away from the solute cloud is reached, which triggers the de-pinning process and results in a significant stress drop (P2 to P3). Due to the high diffusion rate of solute atoms, the dislocation runs into a saturated atmosphere of solute again, bringing the stress back to the general "solute-drag" level of the stress-strain curve (P3 to P4 in Fig. 6b).

When comparing the DSA mechanisms underlying Type A (or B) and Type C serrations, the pinning process drives the onset of Type A (or B) serration since the dislocation velocity must be locally slowed enough before the solute atoms are able to pin it. In contrast, the de-pinning process plays the controlling role for the onset of Type C serration since there are usually ample

solute atoms available to saturate the dislocation core and the mobile dislocations can only break free in brief bursts.

## 4.4. Correlation of dislocation mobility to serration types

As evidenced from Fig. 5, the serration types vary as a function of the imposed strain rate and the accumulation of plastic strain. Essentially, the specific type of serration is a manifestation of a distinctive DSA mechanism that results from the interplay of diffusing solute atoms with gliding dislocations that carry a specific mobility. The solute diffusion rate in our study is invariable as the temperature is kept constant at 600 °C. In contrast, the mobile dislocation velocity (or dislocation mobility) is varied depending on the controlled external strain rate as well as the accumulation of plastic strain. The variety of dislocation mobility alters the solute-dislocation interaction and in turn triggers changes in serration types. Accordingly, there should exist an intrinsic correlation between the average dislocation velocity and serration type.

Following the Orowan equation, the plastic shear strain rate $\dot{\gamma}_p$ is associated with the average velocity of mobile dislocations $\bar{v}_m$ by the expression:

$$\dot{\gamma}_p = \rho_m b \bar{v}_m \, , \qquad \text{Eq. 1}$$

where $\rho_m$ is the mobile dislocation density and $b$ is the Burgers vector magnitude. In view that the mobile dislocation density ($\rho_m$) is at least one order of magnitude less than the total dislocation density ($\rho$) (Ma et al., 2006), we simply assume $\rho_m \approx 0.1\rho$ according to (Ma et al., 2006). Therefore, the average velocity of mobile dislocation ($\bar{v}_m$) can be estimated from the total dislocation density ($\rho$) by rearranging the Orowan equation:

$$\bar{v}_m = \left(M\dot{\varepsilon}_p\right)/(0.1\rho b) \, , \qquad \text{Eq. 2}$$

where $\dot{\varepsilon}_p$ is the plastic strain rate, which is determined directly from the experimental data (Fig. 4) and listed in Table B.2 in Appendix B. $M$ is the Taylor factor, which is taken as 3 for *fcc* metals with a random texture (Taylor, 1934). Based on the framework of the Kocks-Mecking model (Kocks, 1976; Mecking and Kocks, 1981), the evolution of the total dislocation density ($\rho$) can be estimated as a function of the plastic strain at different strain rates (Fig. B.3.b, the detailed calculation can be found in Appendix B). Although alternative approaches using advanced dislocation-based constitutive models (Langer et al., 2010; Le et al., 2017; Le, 2018) are

available, the classical Kocks-Mecking formulation for dislocation evolution (Eq. B.3 in Appendix B) gives a good prediction of the stress-strain response as well as providing the evolution of the dislocation density. By applying Eq. 2, the evolution of the average velocity of mobile dislocations can be obtained with respect to the accumulation of plastic strain at different controlled strain rates. The results are summarized in Fig. 7. Also indicated in this figure are the critical strains and the transformation strains that signifying the onset of serration and the transition between the serration types, respectively.
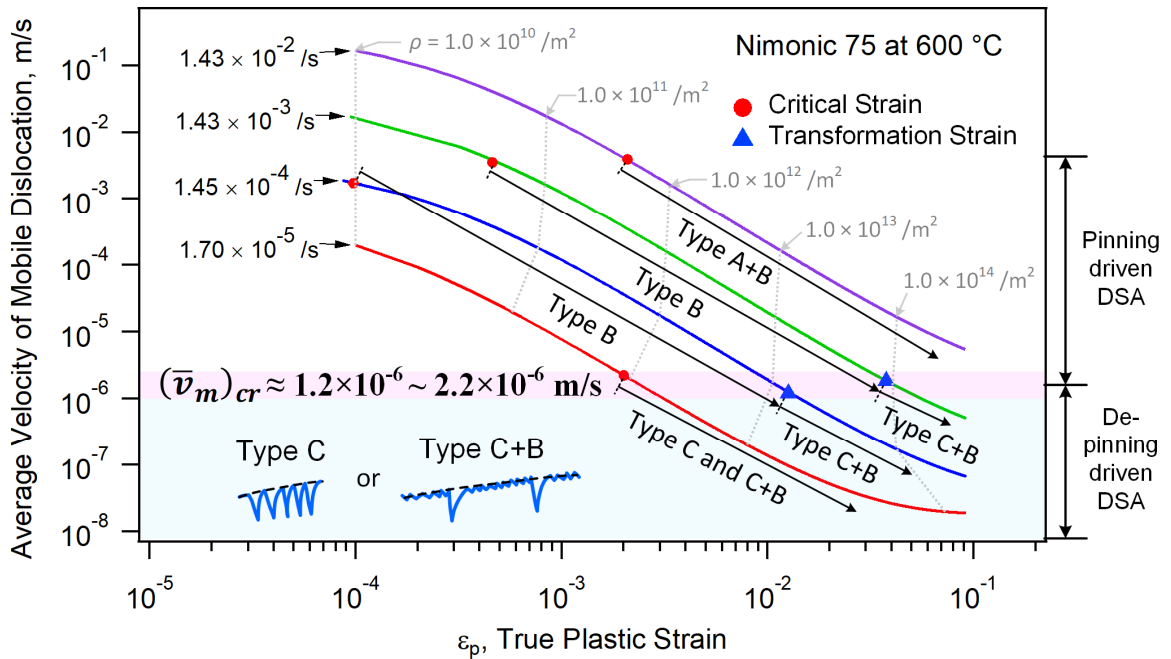


**Fig. 7.** Evolution of the average velocity of mobile dislocations with respect to the accumulation of the plastic strain at different applied strain rates for Nimonic 75 alloy deformed at 600 °C.

It is revealed from Fig. 7 that, regardless of the applied strain rate and the accumulation of plastic strain, the serrated flow will transform to a Type C (or a Type C+B) serration as long as the average velocity of the mobile dislocations is reduced to a *critical dislocation velocity* ($v_m^{cr}$) which falls in the range of $1.2 \times 10^{-6}$ – $2.2 \times 10^{-6}$ m/s. The serration transition behavior is particularly evident when the stress-strain data is plotted in 3-D with mean dislocation velocity on the third axis (Fig. 8a). In Fig. 8a, it becomes clear that in the regions of C (or C+B) type serrations (plotted in red) the flow stress increases with increasing strain rate, but this

relationship is broken at high velocities. Plotting the stress-strain-dislocation density trajectories (Fig. 8b) reveals no correlation between the serration behavior and the dislocation density.
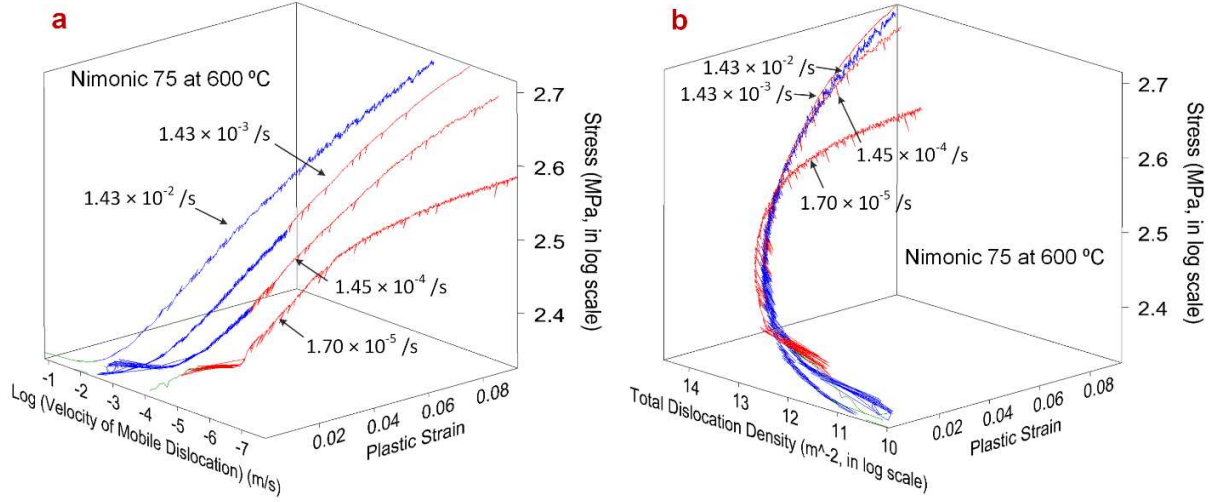


**Fig. 8.** (a) Three-dimensional (3-D) stress-strain-dislocation velocity trajectories for the four different strain rates. The portions of each trajectory in the C (or C+B) serration regime are plotted in red. The portion before the critical strain is plotted in green, and the region between $\varepsilon_{cr}$ and $\varepsilon_{tr}$ is plotted in blue. It can clearly be seen that the portions in red are in a high-solute-drag regime. (b) The stress-strain-dislocation density trajectories plotted using the same color scheme. It can be seen that the onset of viscous behavior with C (or C+B) serrations is independent of the dislocation density.

As schematically illustrated in Fig. 6, the DSA mechanism governing Type C serration is driven by the solute de-pinning process, where dislocations break free from the locking solute cloud with short bursts of deformation. In contrast, the DSA mechanism underlying Type A (or Type B) serration is driven by the solute pinning process. Here it is found that the onset of the de-pinning driven DSA mechanism can be determined by a critical velocity of mobile dislocations ($v_m^{cr}$) at a specific temperature (600 °C in the present work), whereby the solute diffusion rate is considered constant. Significantly, this critical average velocity of mobile dislocations, which is inherently dependent of the solute diffusion rate, can be regarded as a physical DSA parameter that defines the shift in mechanism associated with Type C serration. This raises a key question: What is the physical significance of the average critical dislocation velocity $v_m^{Cr} \sim 1.7$ μm/s in Nimonic 75 deformed at 600 °C?

18

## 4.5. Physical origin of the critical dislocation velocity

### Bulk diffusion model

In established models quantifying the drag on an edge dislocation due to a Cottrell atmosphere, energy is dissipated by *bulk* diffusion of solute to minimize the elastic energy caused by the interaction between the solute's dilatory strain field with the dislocation's long range hydrostatic strain. When the dislocation is moving, solute diffuses to relax towards the moving potential. The net potential energy that is dissipated as the solute diffuses downhill exerts a drag force on the dislocation motion. A one-dimensional scaling analysis of the problem for dilute solutions is provided in (Hirth and Lothe, 1982) and a more complete analysis is provided by (Cottrell and Jaswon, 1949). At slow speeds, the drag force is proportional to the dislocation velocity and is dominated by solute within the diffusion distance, $r_D$, defined as:

$$r_D = \frac{D_L}{v}, \qquad \qquad \text{Eq. 3}$$

where $v$ is the dislocation velocity and $D_L$ is the lattice diffusion coefficient of Cr solute (Table 2). At high dislocation velocities, the excess solute is unable to keep up with the moving dislocation, but there is still bulk solute diffusion in response to the dislocation's strain field as it moves, which causes drag and leaves a wake of perturbed solute behind the dislocation. The transition from diffusion-dominated to drift-dominated drag should occur at a steady state dislocation velocity (Hirth and Lothe, 1982):

$$v_t = \frac{k_B T D_L}{b\, P_o\, \delta\Omega}, \qquad \qquad \text{Eq. 4}$$

where the numerator $k_B T D_L$ is the product of the Boltzmann constant, temperature, and chemical diffusion coefficient of Cr solute, respectively (Table 2). In the denominator, $b$ is the dislocation's Burgers vector magnitude and $P_o = \frac{G}{3\pi}\left(\frac{1+v}{1-v}\right)$ is the amplitude of the pressure field it generates, while $G$ and $v$ are the shear modulus and Poisson ratio, respectively (Table 2). $\delta\Omega$ is the Cr volume dilation, which is 1.75 $\text{Å}^3$ (Table 2). A maximum drag force should be reached at a critical velocity $v_{cr}$ of $4v_t$ (Hirth and Lothe, 1982).

Computing the value of $v_t$ in Nimonic 75 at 600 °C yields $v_t = 4.8{\times}10^{-12}$ m/s and $v_{cr} = 4v_t = 1.9{\times}10^{-11}$ m/s, which is about five orders of magnitude smaller than the critical velocity

(~1.7×10⁻⁶ m/s) experimentally measured in this work for the onset of Type C (or C+B) serration. It should be noted that this value is generated by using the chemical diffusion coefficient of Cr in Ni–20%Cr. One could argue that this underestimates the rate of Cr diffusion in the vicinity of the dislocation as the Cr current flows counter to the flux of vacancies responding to the same stress field, and in regions of tensile stress the activation energy for hopping will be reduced. However, to bring $v_t$ in Eq. 4 to the same magnitude as the critical velocity estimated from our experiments requires reducing the diffusion activation energy by 0.9 eV. This is highly unlikely, which suggests that the mechanism of solute drag in this case is limited not by bulk diffusion around the dislocations, but by pipe diffusion processes. This could be due to pipe diffusion along the pores, or from rearrangement of solute within the core as the dislocation sweeps past. In the sections that follow we examine both possibilities.

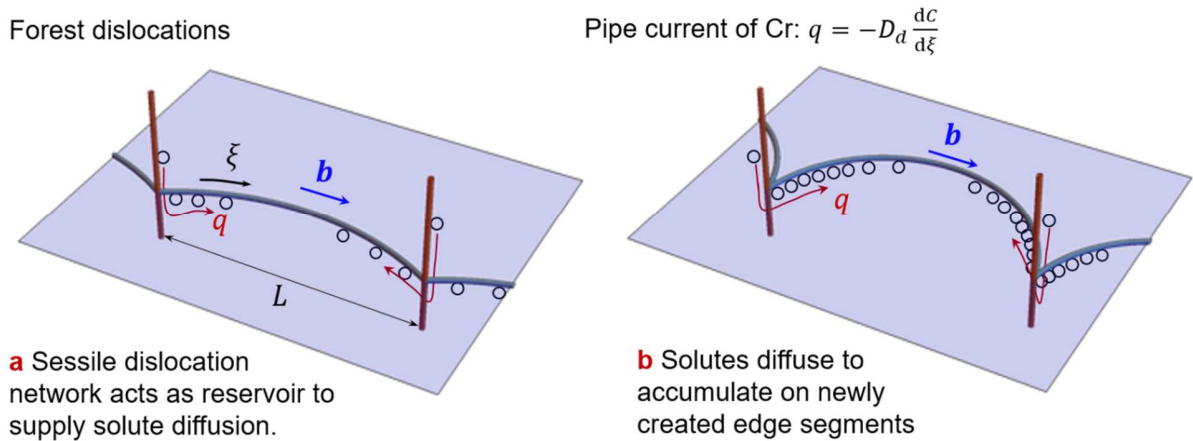*Model of pipe diffusion along dislocations lines*



Forest dislocations

Pipe current of Cr: $q = -D_d \frac{dc}{d\xi}$

**a** Sessile dislocation network acts as reservoir to supply solute diffusion.

**b** Solutes diffuse to accumulate on newly created edge segments

**Fig. 9.** Schematic diagram illustrating the pipe diffusion model used to interpret the physical origin of the critical dislocation velocity. (a) Sessile dislocation network acts as the reservoir to supply solute diffusion. (b) Solutes diffuse to accumulate on newly created edge segments.

Here we examine if a pipe diffusion model can quantitatively describe the critical dislocation velocity at which a dislocation network breaks free from the solute segregated to its core. We hypothesize that this break away moment should occur when pipe diffusion is no longer able to supply enough solute to keep up with the rate of dislocation multiplication. We first consider the relationship between the average dislocation velocity and the rate of increase in

the dislocation density $\dot{\rho}$. The critical resolved shear stress $\tau$ to bow a dislocation between two obstacles with spacing $L$ is given by the well-known equation:

$$\tau = \frac{2bG}{L}, \qquad \text{Eq. 5}$$

where $G$ is the shear modulus and the dislocation line tension is assumed to be $b^2G$. Assuming that the dislocation network multiplies due to pinning by forest dislocations with an average distance between pinning sites of $L = \frac{\alpha}{\sqrt{\rho}}$ (Fig. 9a), where $\alpha$ is a proportionality constant of order unity, following the approach in (Kocks, 1976). The work hardening rate $\Theta$, which originates from the net change in the total dislocation density, can be obtained following:

$$\Theta = \frac{\mathrm{d}\sigma_y}{\mathrm{d}\varepsilon_p} = \frac{\mathrm{d}}{\mathrm{d}\varepsilon_p}\left(\frac{2bG}{L} \times M\right) = \left(\frac{bG}{\alpha}\right)\frac{1}{\sqrt{\rho}}\frac{\mathrm{d}\rho}{\mathrm{d}\varepsilon_p} \times M = \left(\frac{bG}{\alpha}\right)\frac{1}{\sqrt{\rho}}\frac{\dot{\rho}}{\dot{\varepsilon}_p} \times M . \qquad \text{Eq. 6}$$

Substituting for the strain rate using the relationship between the average dislocation velocity and the total dislocation density in Eq. 2 and rearranging, one obtains:

$$\bar{v}_m = \frac{\dot{\rho}}{\rho\sqrt{\rho}}\left(\frac{G}{\Theta}\right)\left(\frac{M^2}{\beta\alpha}\right), \qquad \text{Eq. 7}$$

where $\beta = \frac{\rho_m}{\rho} \approx 0.1$, $\alpha \approx 1$. Eq. 7 gives the net generation rate of new dislocation line. We now consider the solute segregated to the dislocation core, and the rate at which new solute must be supplied to keep up with the generation of new dislocation line. In Nimonic 75, one in five of the atoms in the crystal is chromium, thus Cr atoms do not have to travel far to reach the dislocation core. As Cr is larger than Ni, there is a strong driving force to make all of the atoms at the top of the edge dislocation half plane be Ni, with the Cr atoms just below the half plane. We define the core segregation, $\chi_\xi$, as the fraction of the atomic sites below the half plane of an edge dislocation occupied by Cr. Thus, in a segment of dislocation line of a length $\xi$, $\chi_\xi$ can be expressed by:

$$\chi_\xi = \frac{n_{Cr}}{\xi\, n_\xi}, \qquad \text{Eq. 8}$$

where $n_\xi$ indicates the number of dilatational core sites per unit length of edge dislocation line, and $n_{Cr}$ is the number Cr atoms occupying them. At equilibrium we expect the core to be fully decorated with Cr so that for stationary edge dislocations $\chi_\xi \approx 1$. For fast moving dislocations

that have broken free from their solute, $\chi_\xi$ is the nominal alloy composition $\chi_0$, which in Nimonic 75 is 0.2. During plastic deformation, generation of new edge dislocation length dilutes the concentration of Cr on the mobile segments at an average rate of:

$$\dot{\chi}_\xi = -\frac{1}{2}\chi_\xi \frac{\dot{\rho}}{\rho_m} , \qquad \text{Eq. 9}$$

where the one half comes from assuming that on average halve of the generated dislocation is edge character. If this solute is supplied *solely* from pipe diffusion from the pinned ends of the mobile segment as depicted in Fig. 9, this demands a current of, $q$, solute atoms per second in from the end of:

$$q = \frac{1}{4}n_\xi\alpha\big(\chi_\xi - \chi_o\big)\frac{\dot{\rho}}{\rho_m\sqrt{\rho}} = \frac{1}{4}\Big(\frac{\Theta}{G}\Big)\Big(\frac{\alpha^2}{M^2}\Big)\big(\chi_\xi - \chi_o\big)n_\xi\bar{v}_m . \qquad \text{Eq. 10}$$

This relationship indicates that the solute current along mobile dislocations depends on the mean dislocation velocity, independent of the dislocation density. It suggests that the critical velocity below which the system transitions to viscous drag with intermittent break away events causing C-type serrations is set by the maximum solute current that the dislocation cores can transport. Or mathematically, for C-type serrations we have the inequality:

$$q_{max} > \frac{1}{4}\Big(\frac{\Theta}{G}\Big)\Big(\frac{\alpha^2}{M^2}\Big)\big(\chi_\xi - \chi_o\big)n_\xi\bar{v}_c . \qquad \text{Eq. 11}$$

An order of magnitude estimate for the maximum solute current that can be supplied by considering the pipe diffusion equation is:

$$q = -D_d\frac{dC}{d\xi} , \qquad \text{Eq. 12}$$

where $q$ is the net number of Cr atoms passing along a dislocation per unit time, $D_d$ is the pipe diffusion coefficient (with units of m⁴s⁻¹) (Table 2), and $\frac{dC}{d\xi}$ is the gradient in the bulk concentration of solute $C$ along the direction of the dislocation line. The pipe diffusion coefficient has typical Arrhenius dependence of temperature $T$, and activation energy $Q$, with $D_d = D_o e^{-\frac{Q_d}{k_B T}}$. Frost and Ashby have reported values for $Q_d$ and $D_o$ determined from power law creep experiments (Frost and Ashby, 1982) (Table 2). If we assume that the gradient in bulk concentration can be interchanged with the gradient in core concentration, then we may estimate

the pipe current due to the core becoming depleted of solute over a characteristic diffusion length $d$ as $q = D_d(\chi_\xi - \chi_o)\frac{n_\xi}{A\,d}$. Combining this relationship with the inequality in Eq. 11 gives an expression for the critical velocity for the onset of viscous drag:

$$\bar{v}_{cr} = 4\frac{D_d}{d\,A}\left(\frac{G}{\Theta}\right)\left(\frac{M^2}{\alpha^2}\right).$$  Eq. 13

As the diffusion length will be related to the segment length, this condition means that the critical velocity is not independent of the dislocation density, as is observed in experiments. This mechanism, therefore, cannot be responsible for the drag behavior when Type-C serrations occur. Moreover, if we assume that $A \approx 2b_p^2$, where $b_p$ is the burgers vector of the partial dislocation, and use the parameters in Table 2, the experimentally measured critical speed of $\bar{v}_{cr} = 1.7\ \mu$m/s will correspond to a diffusion length of ~ 170 nm. This is an order of magnitude larger than the mean segment length when the alloy strained at $1.43\times10^{-3}$ s$^{-1}$ transitions to the viscous regime with C-type serrations.

*Model of solute rearrangement across dislocation cores*

An alternative model is to consider that dislocations have no accumulated core segregation, but time is taken for solute atoms to hop from above to below the glide plane across the core as the dislocation core moves past the solute atom, as illustrated in Fig. 10. This is similar in concept to the "cross-core" mechanism of Curtin (Curtin et al., 2006). Here, rather than considering the drag imposed by this mechanism, we focus solely on obtaining an estimate for the relaxation time for solute core-crossing and relating it to a critical dislocation velocity.
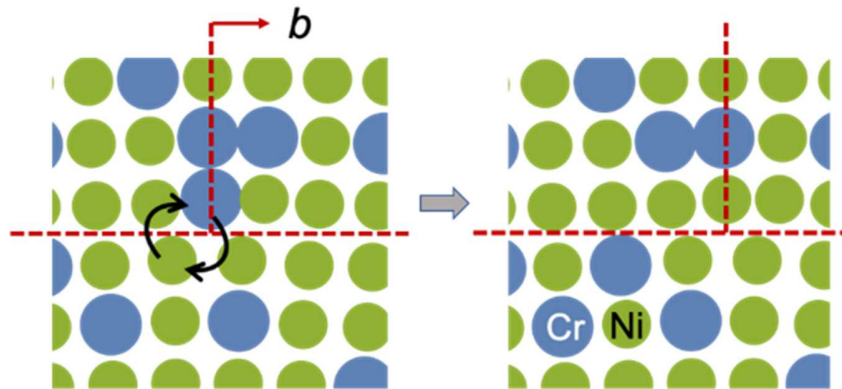
**Fig. 10.** Schematic of a solute atom hopping from above to below the glide plane across the core as an edge dislocation passes.

From the pipe diffusion equation one can compute the attempt frequency for core atoms hopping as $\Gamma = \frac{D_o}{\eta \, b^2 b_p^2}$, where the full Burgers vector $b$ gives the atomic jump distance along the dislocation line, $b_p^2$ is the cross-sectional area of a single partial dislocation core, and $\eta$ is a numerical factor that accounts for the available hopping directions and correlation effects. The probability that a hop is successful is the Boltzmann factor with the activation energy for pipe diffusion $e^{\frac{-Q_d}{k_B T}}$. The $\Delta t$ is the average time it takes a solute atom to hop across the dislocation core from the compressive to tensile sides (from above to below the glide plane in Fig. 10) as a partial dislocation core sweeps through the lattice. It is the reciprocal of the rate of hopping: $\Delta t^{-1} = \eta \Gamma \, e^{\frac{-Q_d}{k_B T}}$. If this process is to create a drag on the dislocation, the dislocation must be moving slow enough that the hoping time is less that the time it takes for the dislocation core to pass by. If we equate the hoping time to the time that it takes for the passage of two partial dislocation cores, we obtain the critical velocity:

$$v_{cr} = 2\frac{b_p}{\Delta t} = 2\frac{D_p}{b_p b^2}.$$

Eq. 14

Again, using the values from Table 2, this core hopping model predicts a critical velocity of 1.1 $\mu$m/s, remarkably close to the lower end of the range of experimentally observed critical velocities. As this is not expected to be a quantitively exact model, the high quality of agreement is probably fortuitous. More importantly, the agreement is of the correct order of magnitude, and many orders of magnitude closer that the other two models considered, thus giving confidence in the mechanistic description.

From the three models of solute motion examined above, we conclude that the minor rearrangement of solute across the glide plane in the dislocation core as the dislocation glides through the lattice is responsible for the viscous behavior that gives rise to Type-C serrations in the stress-strain curve. Of the three potential solute drag mechanisms considered, this is the only one that can both operate at the experimentally observed dislocation speeds and is independent of dislocation density. Although performing experiments at other temperatures was beyond the scope of this current study, this hypothesis could be tested in the future by performing tensile

tests at higher temperatures in which case one would expect the onset of C-type serrations occurring at earlier critical strains, with the critical dislocation velocity having Arrhenius temperature scaling with activation energy of 1.76 eV.

**Table 2** Physical quantities of Ni-20Cr alloy used to derive the theoretical critical dislocation velocity.

| Physical quantities | Symbol | Value | Unit |
|---|---|---|---|
| Ni atomic volume | $\Omega_{Ni}$ | 10.71 | Å$^3$ |
| Cr atomic volume | $\Omega_{Cr}$ | 12.46 | Å$^3$ |
| Cr volume dilation | $\delta\Omega$ | 1.75 | Å$^3$ |
| Burgers vector | $b$ | 2.49 | Å |
| Burgers vector for a partial dislocation | $b_p$ | $b/\sqrt{3}$ | Å |
| Shear modulus | $G$ | 63 | GPa |
| Poisson ratio | $\nu$ | 0.34 | — |
| Cr lattice diffusion coefficient | $D_L$ | $v_h e^{-Q_L/k_B T}$ | m$^2$/s |
| Cr lattice diffusion attempt frequency | $v_h$ | 1.9×10$^{-4}$ | m$^2$/s |
| Cr lattice diffusion activation energy | $Q_L$ | 2.93 | eV |
| Cr pipe diffusion coefficient | $D_d$ | $D_o e^{-Q_d/k_B T}$ | m$^4$/s |
| Cr pipe diffusion prefactor | $D_o$ | 1×10$^{-25}$ | m$^4$/s |
| Cr pipe diffusion activation energy | $Q_d$ | 1.76 | eV |
| Boltzmann constant | $k_B$ | 1.38×10$^{-23}$ | m$^2$ kg s$^{-2}$ K$^{-1}$ |
| Temperature | $T$ | 873 | K |
| Work hardening rate | $\Theta$ | 4.1 | GPa |
| Mobile dislocation fraction | $\beta$ | 0.1 | — |
| Pipe cross-sectional area | $A$ | $a^2$ | |
| Lattice parameter | $a$ | 3.52 | Å |

## 5. Conclusions

Monotonic tension tests were performed at 600 ℃ at four constant strain rates 1.43×10$^{-2}$ /s, 1.43×10$^{-3}$ /s, 1.45×10$^{-4}$ /s, and 1.70×10$^{-5}$ /s to study the effects of both strain rates and

accumulated plastic strain on the serrated plastic flow behavior of Nimonic 75 alloy. The following conclusions are drawn:

1. Serrated flow occurs at all of the applied strain rates. When the strain rate is increased from $1.70 \times 10^{-5}$ /s up to $1.43 \times 10^{-2}$ /s, the critical strain first exhibits an inverse behavior, decreasing with increasing strain rate, and later a normal behavior, increasing with increasing strain rate.

2. Decreasing the strain rate from high-strain-rate regime to low-strain-rate regime results in a transformation of the serration type from Type A+B, through Type B, and to Type C. With accumulation of plastic strain at the intermediate and low strain rates, Type B and Type C serrations transform to a Type C+B serration.

3. A critical average velocity of mobile dislocations ($v_m^{cr}$) was found that defines the onset of the transition to a Type C serration de-pinning dominated process. This transition velocity was quantitatively associated with the rate of solute transfer across the glide plane in the dislocation core as the dislocation glides through the lattice.

**Appendix A. Extracting the Young's modulus and the elastic proportional limit**

No standardized procedures exist to select the linear portion of the stress-strain curve for fitting Young's modulus to identify the proportional limit. Here we linearly fit the stress-strain data in increasingly larger sections of data starting from zero stress to a "high-bound" stress level using the least squares method. By fixing the starting point (zero stress) and increasing the "high-bound" stress level, a series stress-strain sections were fit to obtain the regression line slope and the coefficient of determination $R^2$ as a function of the increasing "high-bound" stress level (Fig. A.1). As a higher $R^2$ indicates better fitting, the "high-bound" stress corresponding to the maximum $R^2$ was taken as the proportional limit (Fig. A.1). The associated slope of the regression line at the maximum $R^2$ was taken as the Young's modulus for the specific loading condition.
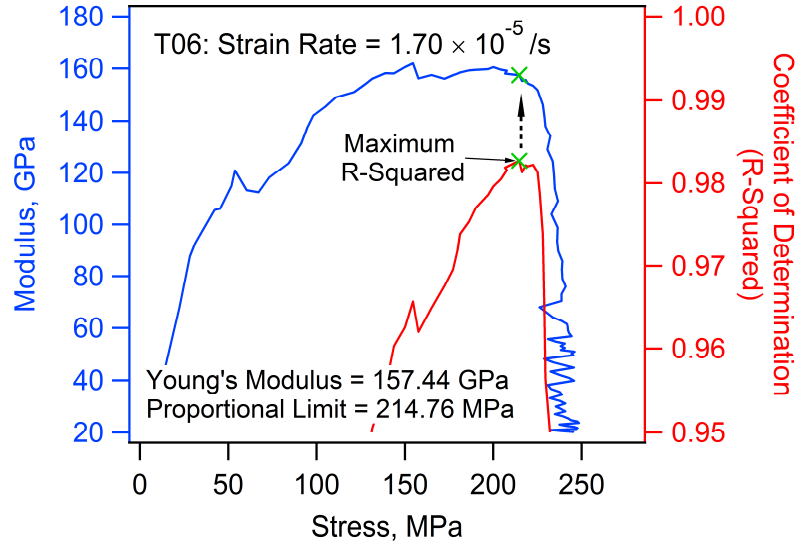
**Fig. A.1.** Determination of the Young's modulus and the proportional limit by finding the maximum value of the coefficient of determination ($R^2$) as a function of the "high-bound" stress level in the fitting section.

## Appendix B. Estimating the evolution of total dislocation density

The Kocks-Mecking model (Kocks, 1976; Mecking and Kocks, 1981) is a constitutive modeling approach that takes account of the dislocation density as an internal variable to represent the microstructural state of a material. The framework of Kocks-Mecking model (Kocks, 1976; Mecking and Kocks, 1981) takes into account a decomposition of the flow stress into two components:

$$\sigma_f = \sigma_0 + \sigma_d \ , \qquad \text{Eq. B.1}$$

where $\sigma_f$ is the flow stress. The component $\sigma_0$ is a short-range stress signifying the onset of dislocation slips and can be practically identified as the proportional limit, which was determined to be 211 MPa for Nimonic 75 at 600 °C. The component $\sigma_d$ is a strain-dependent stress originated from the long-range interaction between dislocations. $\sigma_d$ is formulated as a function of the total dislocation density according to Taylor's equation (Taylor, 1934):

$$\sigma_d = \alpha M G b \sqrt{\rho} \ , \qquad \text{Eq. B.2}$$

where $G$ represents the shear modulus, which is determined as 63 GPa from the Young's modulus (168.1 GPa) assuming a Poisson's ratio of 0.34. $b$ is the magnitude of Burgers vector

27

characterized by the equation: $b = \frac{a}{2}\sqrt{1^2 + 1^2 + 0^2} = 2.49 \times 10^{-10}\ m$, where $a$ is the lattice parameter taken to be 3.52 Å for Nimonic 75 (Ni-20Cr alloy). $M$ is the Taylor factor, which is 3 for *fcc* metals (Taylor, 1934) and $\rho$ is the total dislocation density. Since the as-received material was annealed at 600 °C for 400 hours, the initial dislocation density ($\rho_0$) was assumed to be $1.0 \times 10^{10}\ m^{-2}$, which is a lower-bound value of the dislocation density for annealed metal alloys (Abbaschian et al., 2008). $\alpha$ is a geometrical factor that describes the dislocation interaction (Mughrabi, 2016). The $\alpha$-factor falls in a range varying from 0.1 to 0.8 for different metal alloys (Mughrabi, 2016). At small plastic strain where the dislocations are homogeneously distributed, the $\alpha$-factor can be assumed to be 0.35 (Mughrabi, 2016). The material constants used in the current Kocks-Mecking model for Nimonic 75 alloy are summarized in Table B.1.

**Table B.1** Material constants used in the Kocks-Mecking model for Nimonic 75 alloy.

| $\sigma_0$ (MPa) | $\alpha$ | $M$ | $G$ (GPa) | $b$ ($\times 10^{-10}$ m) | $\rho_0$ (m$^{-2}$) | $\sigma_{d0} = \alpha MGb\sqrt{\rho_0}$ (MPa) |
|---|---|---|---|---|---|---|
| 211 | 0.35 | 3 | 63 | 2.49 | $1.0 \times 10^{10}$ | 1.65 |

With the development of plastic deformation, the accumulation of the total dislocation density results from the competition between the dislocation production/storage and dislocation annihilation. Accordingly, the evolution law of the total dislocation density can be expressed as:

$$\frac{d\rho}{d\varepsilon_p} = \frac{d\rho}{d\varepsilon_p}^+ - \frac{d\rho}{d\varepsilon_p}^- \ , \qquad\qquad \text{Eq. B.3}$$

where $d\rho/d\varepsilon_p^+$ and $d\rho/d\varepsilon_p^-$ represent the work hardening term and the dynamic recovery term, respectively. The original Kocks-Mecking model (Kocks, 1976), Eq. B.3 assumes the form:

$$\frac{d\rho}{d\varepsilon_p} = M\left(k_1\sqrt{\rho} - k_2\rho\right), \qquad\qquad \text{Eq. B.4}$$

where $k_1$ and $k_2$ are two material parameters that account for the work hardening effect and the dynamic recovery effect, respectively. Combining Eqs. B.2 and B.4, we obtain:

$$\sigma_d \frac{d\sigma_d}{d\varepsilon_p} = \frac{M}{2}\left(\alpha MGbk_1\sigma_d - k_2\sigma_d{}^2\right). \qquad\qquad \text{Eq. B.5}$$

Eq. B.5 can be used to obtain the parameters $k_1$ and $k_2$ by fitting the $\sigma_d \frac{d\sigma_d}{d\varepsilon_p}$ vs. $\sigma_d$ curve using the second-order polynomial function.
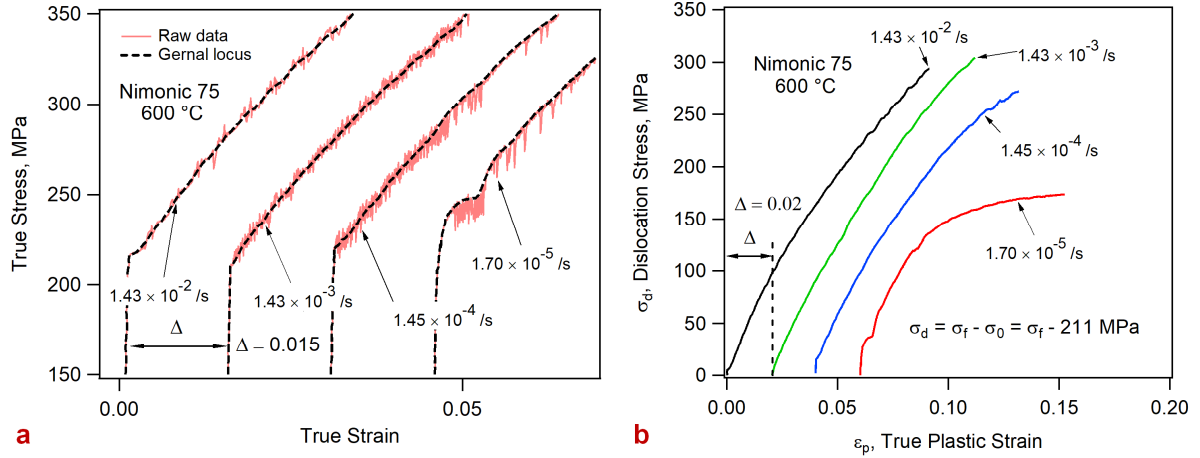


**Fig. B.1.** (a) The representative general true stress-true strain loci extracted from the serrated plastic flow for Nimonic 75 alloy. (b) The representative dislocation stress-true plastic strain curves.

Fig. B.1 presents the representative general true stress-true strain loci extracted from the serrated plastic flows based on their serration types identified in Fig. 4. Fig. B.1b plots the variation of dislocation stress with respect to the true plastic strain. The dislocation stress ($\sigma_d$) was obtained by subtracting the proportional limit ($\sigma_0$) from the flow stress ($\sigma_f$) following Eq. B.1. The true stress at a small plastic strain (0.0001) was chosen as the starting point of the flow stress.
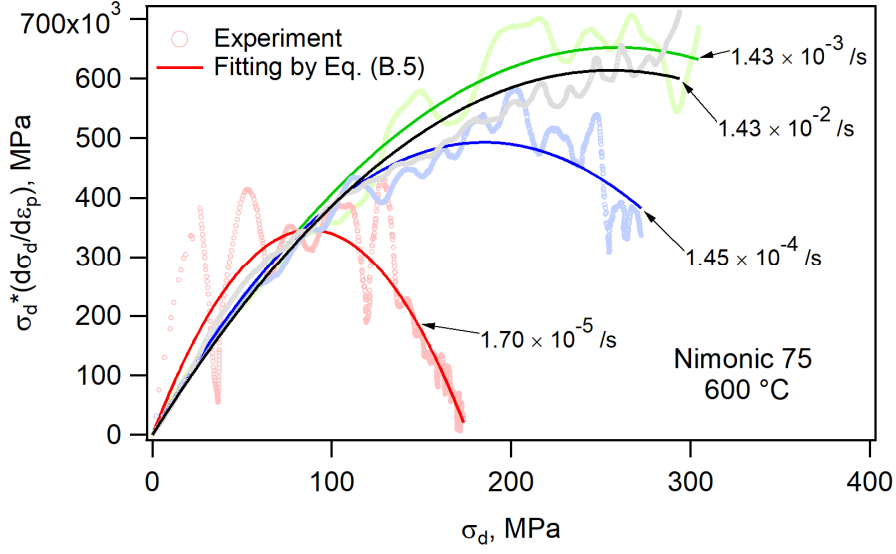
**Fig. B.2.** The experimental $\sigma_d \frac{d\sigma_d}{d\varepsilon_p}$ vs. $\sigma_d$ curves together with the fitting lines using Eq. B.5.

**Table B.2.** The fitted $k_1$ and $k_2$ parameters and the saturated dislocation stress ($\sigma_{dsat}$).

| $\dot{\varepsilon}$ (/s) | $\dot{\varepsilon}_p$ (/s) | $k_1$ ($\times 10^8$ m$^{-1}$) | $k_2$ | $k_1/k_2 = \sqrt{\rho_{sat}}$ ($\times 10^7$ m$^{-1}$) | $\sigma_{dsat} = \alpha MGb(k_1/k_2)$ (MPa) |
|---|---|---|---|---|---|
| $1.43 \times 10^{-2}$ | $1.37 \times 10^{-2}$ | 1.94 | 6.26 | 3.10 | 510.6 |
| $1.43 \times 10^{-3}$ | $1.36 \times 10^{-3}$ | 2.04 | 6.49 | 3.14 | 517.2 |
| $1.45 \times 10^{-4}$ | $1.43 \times 10^{-4}$ | 2.16 | 9.61 | 2.25 | 370.6 |
| $1.70 \times 10^{-5}$ | $1.63 \times 10^{-5}$ | 3.15 | 29.39 | 1.07 | 176.2 |

To fit $k_1$ and $k_2$, we further plot out the $\sigma_d \frac{d\sigma_d}{d\varepsilon_p}$ vs. the $\sigma_d$ curves (Fig. B.2). The fitted lines using Eq. B.5 are displayed in Fig. B.2 as well. The fitted $k_1$ and $k_2$ are listed in Table B.2. Also listed in Table B.2 is the saturated dislocation stress:

$$\sigma_{dsat} = \alpha MGb(k_1/k_2). \qquad \text{Eq. B.6}$$

The saturation of dislocation stress is attained when a balance of the dislocation production/storage and the dislocation annihilation is reached, *i.e.* the dislocation density reaches a saturation value ($\rho_{sat}$), where $d\rho/d\varepsilon_p = 0$ and $\rho_{sat} = (k_1/k_2)^2$.
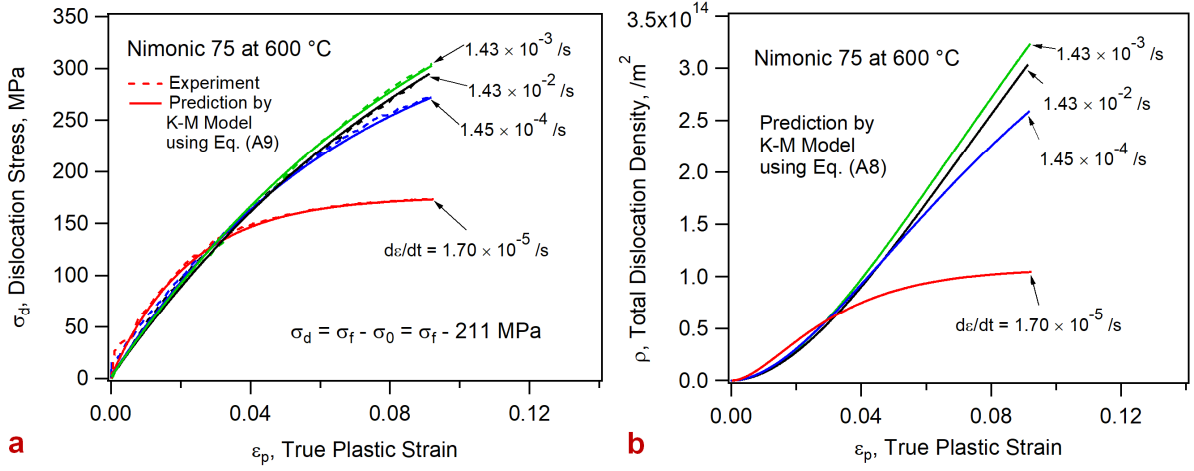
**Fig. B.3.** (a) Comparison of the experimental dislocation stress *vs.* the true plastic strain curves and the predictions by the Kocks-Mecking model. (b) Evolutions of the total dislocation density as a function of the plastic strain and the controlled strain rates.

An analytical solution can be obtained from the differential equation Eq. B.4 for the total dislocation density as a function of the plastic strain:

$$\frac{\sqrt{\rho}-k_1/k_2}{\sqrt{\rho_0}-k_1/k_2} = e^{-\frac{M}{2}k_2(\varepsilon_p-\varepsilon_{p0})}. \qquad \text{Eq. B.7}$$

Substitute Eq. B.2 into Eq. B.7, we obtain the dislocation stress as a function of the plastic strain:

$$\frac{\sigma_d-\sigma_{dsat}}{\sigma_{d0}-\sigma_{dsat}} = e^{-\frac{M}{2}k_2(\varepsilon_p-\varepsilon_{p0})}. \qquad \text{Eq. B.8}$$

In Eqs. B.7 and B.8, $\varepsilon_{p0}$ is taken as a small value of 0.0001. $\sigma_{d0}$ (1.65 MPa) is the initial dislocation stress determined by the initial dislocation density ($\rho_0 = 1.0 \times 10^{10}\ m^{-2}$) (Table B.1), whereas $\sigma_{dsat}$ indicates the saturated dislocation stress (Table B.2). The dislocation stress *vs.* the true plastic strain curves predicted by the Kocks-Mecking model (Eq. B.8) show good agreement with the experimental data (Fig. B.3a). The evolution of the total dislocation density as a function of the accumulated plastic strain and the controlled strain rates were then obtained from Eq. B.7, as shown in Fig. B.3b. The estimated evolution of total dislocation density was used to derive the average velocity of mobile dislocations in Section 4.4.

**Appendix C. Mathematical approach to identify the serration transition from Type B to Type C+B**

To verify the results obtained by direction observation, we have developed a robust numerical algorithm to identify the transition in behavior from Type B to Type B+C serration. This procedure mathematically defines the process that we previously performed by direction observation and yields the same results. The C type serrations are brief involving only between 3-5 data points depending on the strain rate. However, they have a distinct asymmetry, both in stress (the serration is a drop in stress rather than an oscillation of the stress) and in strain (the serration drops sharply but rises more smoothly). This characteristic shape means that it is possible to devise a kernel function or wavelet envelope that can be convoluted with the stress noise and the filtered signal used to identify instances of C-type serrations. We have done this, and while this beautifully reveals the location of *individual* C type serrations in the C+B regime, it is not very useful for identifying the onset of the C+B regime as this algorithm can only locate those standalone C serrations which are distributed sparsely throughout this region. However, the first instance of a C-type serration often occurs and connects to the last serration of B type. To overcome these difficulties, our approach involves three steps (Fig. C.1): (1) extracting the stress noise from the true stress in the stress-strain curve, and then using two signal processing algorithms on this noise to (2) identify if C+B serrations do occur, and (3) to quantify the strain at which the transition takes place.
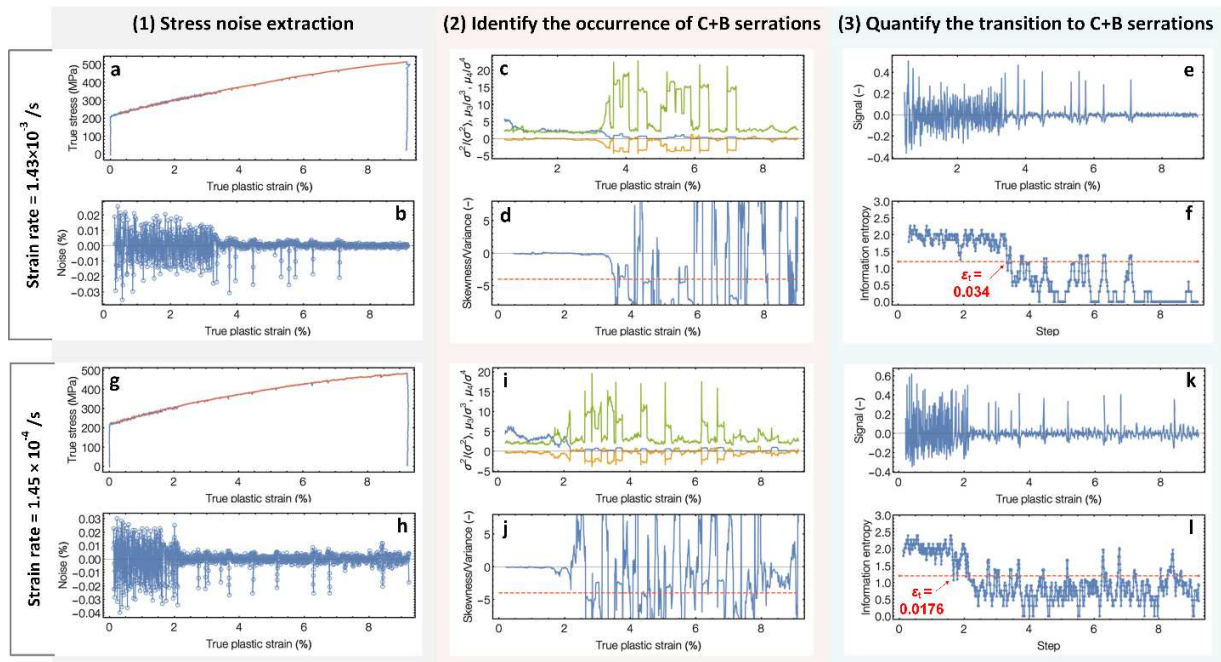


32

**Fig. C.1.** Numerical algorithm to identify the transition in behavior from type B to type B+C serration for strain rates at (a-f) $1.43 \times 10^{-3}$ /s and (g-l) $1.45 \times 10^{-4}$ /s.

**(1) Stress noise extraction:** The stress fluctuations are defined as the stress excursions from a $2^{nd}$ order polynomial fit to the stress-strain curve in a moving local window. This approach allows us a wide moving window (of 41 data points, or a strain range of 0.38-0.25% depending on the strain rate) for noise cancelation while acknowledging the slope and curvature of the stress-strain profile. Mathematically we define the fractional stress noise, $\eta_i$, of the $i$th strain point as:

$$\eta_i = \frac{\sigma_i - \widetilde{\sigma_\iota}}{\widetilde{\sigma_\iota}}, \qquad\qquad \text{Eq. C.1}$$

where $\widetilde{\sigma_\iota}$ is the *general* stress, or the stress value predicted at strain $\varepsilon_i$ by a $2^{nd}$ order polynomial fit to the stresses from the $i - n$ to $i + n$ data points with $n = 20$ in our implementation. Figs. C.1a and g show the stress-strain data (in blue) along with the general stress plotted in red. The obtained noise $\eta$ is plotted in Figs. C.1b and h for the strain rates at $1.43 \times 10^{-3}$ /s and $1.45 \times 10^{-4}$ /s, respectively.

**(2) Identify the occurrence of C+B serrations:** The transition from the B type to C+B type regime is marked by two characteristics: a large reduction in the amplitude of the symmetric B-type serrations, and the intermittent occurrence of C-type serrations. The reduction in B-type serration amplitude gives a reduction in the local variance of the stress noise. The occurrence of C-type serrations will lead to *negative skewness* ($s_i$) of the local stress noise distribution. As a metric that reflects both of these, we consider the skewedness/variance ratio:

$$R_i = s_i / v_i^*, \qquad\qquad \text{Eq. C.2}$$

where $s_i$ is the skewedness of the stress noise in a narrow moving window centered at $\varepsilon_i$, and $v_i^* = v_i / \langle v \rangle$ is the variance of the noise, $v_i$, in the same window normalized by the mean variance, $\langle v \rangle$, of $\eta_i$ over the entire stress-strain curve. We found that a moving window of 30 data points was sufficient to provide meaningful sampling of the stress while also providing a relatively localized metric. We set as the threshold that type C+B serrations have become active if the skewedness/variance ratio $R_i$ becomes less than -4, meaning a halving of the noise variance and doubling the skewedness. The negative sign discriminates for the downward direction of the

C-type serrations. In Figs. C.1e and i, the local normalized variance $v^*$, skewedness $s$, and kurtosis are plotted respectively in blue, gold, and green colors. The skewedness/variance ratio $R$ is plotted in Figs. C.1d and j along with the $R = -4$ threshold shown with the dashed red line.

**(3) Quantify the strain at the transition to C+B serrations:** While the occurrence of the first standalone C-type serration makes the skewedness become large and negative, there is a long variable wait time to observe the change in $R$. Thus, the skewedness/variance metric $R$ is not useful for identifying exactly *where* the transition occurred, only that it has occurred. To pin down the transition strain more closely, we use a signal processing metric that identifies changes in signal texture—the *Shannon information entropy* (Shannon, 1948). This is a measure of how many elements in a string have the same value regardless of the what the values are and how they are ordered in the string. For a signal of length $n$ data points that together have $b$ unique values, the information entropy is defined as:

$$S = \sum_{j=1}^{b} p_j \ln[p_j] \, , \qquad\qquad \text{Eq. C.3}$$

where $p_j$ is the fraction of the signal's $n$ elements that have the $j$th unique signal value. To compute this with our stress noise, we first scaled and discretized the noise by rounding the noise values to a single significant digit (making $b = 10$), before passing through a moving information entropy filter with a moving window of $n = 11$ points in the noise signal. When the information entropy dipped below 1.25 the transition from B to C+B serrations was deemed to occur, providing that the skewedness/variance ratio drops below -4 sometime later. Figs. C.1f and l show $\eta$ filtered by the moving Shannon entropy filter, along with the 1.25 cutoff shown with the dashed red line. For completeness, Figs. C.1f and l show the noise signal obtained from the cross correlation of the noise with a Type-C serration shaped kernel.

As shown in Figs. C.1f and l, the transition strains from Type B to Type C+B serration obtained by the above numerical algorithm are 0.034 and 0.0176 for strain rates at $1.43\times10^{-3}$ /s and $1.45\times10^{-4}$ /s, respectively, which are very close to the 0.033 and 0.0155 obtained by the direct observation method in Figs. 4b and c. This indicates the direct observation method to find the transition strain by inspecting the difference in the characteristic shape of the stress rise and drop between Type B and Type is reliable. The direct observation method is used predominantly throughout the literature for identifying serration types.

**References:**

Abbaschian, R., Abbaschian, L., Reed-Hill, R.E., 2008. Physical Metallurgy Principles. CL-Engineering.

ASTM International, 2009. E21: Standard Test Methods for Elevated Temperature Tension Tests of Metallic Materials. West Conshohocken, PA. https://doi.org/10.1520/E0021-09.2

ASTM International, 2009a. E8. Standard Test Methods for Tension Testing of Metallic Materials. West Conshohocken, PA. https://doi.org/10.1520/E0008

Betteridge, W., Heslop, J., 1974. The Nimonic Alloys and Other Nickel-Base High-Temperature Alloys. Crane, Russak, & Company, Inc., New York.

Bian, X., Yuan, F., Wu, X., 2017. Correlation between strain rate sensitivity and characteristics of Portevin-LeChátelier bands in a twinning-induced plasticity steel. Mater. Sci. Eng. A 696, 220–227. https://doi.org/10.1016/j.msea.2017.04.078

Carroll, R., Lee, C., Tsai, C.-W., Yeh, J.-W., Antonaglia, J., Brinkman, B.A.W., LeBlanc, M., Xie, X., Chen, S., Liaw, P.K., Dahmen, K.A., 2015. Experiments and Model for Serration Statistics in Low-Entropy, Medium-Entropy, and High-Entropy Alloys. Sci. Rep. 5, 16997. https://doi.org/10.1038/srep16997

Cottrell, A.H., Bilby, B.A., 1949. Dislocation theory of yielding and strain ageing of iron. Proc. Phys. Soc. Sect. A 62, 49–62. https://doi.org/10.1088/0370-1298/62/1/308

Cottrell, A.H., Jaswon, M.A., 1949. Distribution of solute atoms round a slow dislocation. Proc. R. Soc. London. Ser. A. Math. Phys. Sci. 199, 104–114. https://doi.org/10.1098/rspa.1949.0128

Cuddy, L.J., Leslie, W.C., 1972. Some aspects of serrated yielding in substitutional solid solutions of iron. Acta Metall. 20, 1157–1167. https://doi.org/10.1016/0001-6160(72)90164-2

Curtin, W.A., Olmsted, D.L., Hector, L.G., 2006. A predictive mechanism for dynamic strain ageing in aluminium-magnesium alloys. Nat. Mater. 5, 875–880. https://doi.org/10.1038/nmat1765

Frost, H.J., Ashby, M.F., 1982. Deformation-mechanism Maps: The Plasticity and Creep of Metals and Ceramics. Elsevier Science Limited.

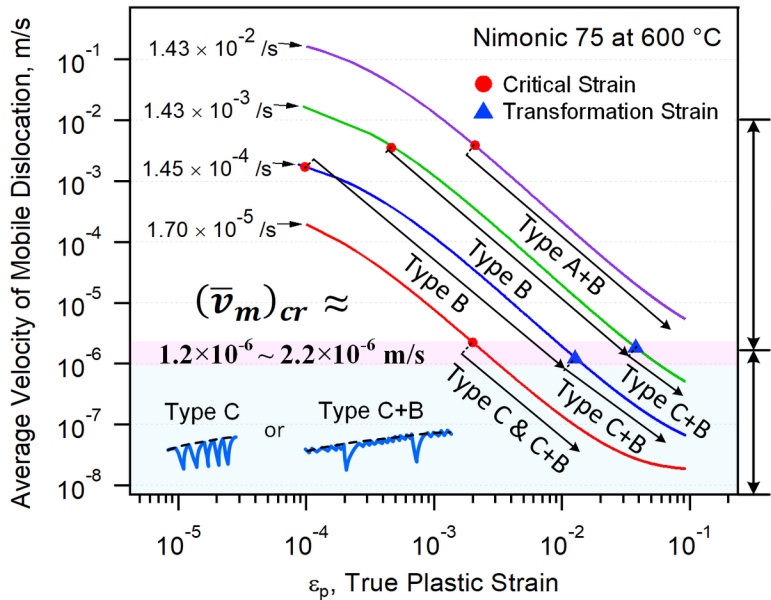Fu, S., Cheng, T., Zhang, Q., Hu, Q., Cao, P., 2012. Two mechanisms for the normal and inverse

behaviors of the critical strain for the Portevin-Le Chatelier effect. Acta Mater. 60, 6650–6656. https://doi.org/10.1016/j.actamat.2012.08.035

Gopinath, K., Gogia, A.K., Kamat, S.V., Ramamurty, U., 2009. Dynamic strain ageing in Ni-base superalloy 720Li. Acta Mater. 57, 1243–1253. https://doi.org/10.1016/j.actamat.2008.11.005

Gould, D., Loveday, M.S., 1990. The certification of nimonic 75 alloy as a creep reference material : CRM 425. Office for Official Publications of the European Communities, Brussels.

Guo, Z.L., Saunders, N., Miodownik, A.P., Schille, J.P., 2007. Quantification of High Temperature Strength of Nickel-Based Superalloys. Mater. Sci. Forum 546–549, 1319–1326. https://doi.org/10.4028/www.scientific.net/MSF.546-549.1319

Hall, E.O., 1970. Yield Point Phenomena in Metals and Alloys. Plenum Press, New York.

Han, G.-M., Tian, C.-G., Cui, C.-Y., Hu, Z.-Q., Sun, X.-F., 2015. Portevin–Le Chatelier Effect in Nimonic 263 Superalloy. Acta Metall. Sin. (English Lett. 28, 542–549. https://doi.org/10.1007/s40195-015-0230-z

Han, G.M., Tian, C.G., Chu, Z.K., Cui, C.Y., Hu, Z.Q., Sun, X.F., 2015. Activation Energy Calculations for the Portevin–Le Chatelier Effect in Nimonic 263 Superalloy. Metall. Mater. Trans. A 46, 4629–4635. https://doi.org/10.1007/s11661-015-3000-7

Hayes, R.W., Azzarto, F., Klopfer, E.A., Crimp, M.A., 2017. Characterization of creep deformation of Ni-Cr solid solution alloy Nimonic 75. Mater. Sci. Eng. A 690, 453–462. https://doi.org/10.1016/j.msea.2017.02.097

Hirth, J.P., Lothe, J., 1982. Theory of Dislocations, A Wiley-Interscience publication. Wiley.

Hong, S.G., Lee, S.B., 2005. Mechanism of dynamic strain aging and characterization of its effect on the low-cycle fatigue behavior in type 316L stainless steel. J. Nucl. Mater. 340, 307–314. https://doi.org/10.1016/j.jnucmat.2004.12.012

Ingelbrecht, C., Loveday, M.S., 2000. The Certification of Ambient Temperature Tensile Properties of a Reference Material for Tensile Testing According to EN 10002-1: CRM 661.

Kocks, U.F., 1976. Laws for Work-Hardening and Low-Temperature Creep. J. Eng. Mater. Technol. 98, 76. https://doi.org/10.1115/1.3443340

Komarasamy, M., Alagarsamy, K., Mishra, R.S., 2017. Serration behavior and negative strain rate sensitivity of Al0.1CoCrFeNi high entropy alloy. Intermetallics 84, 20–24.

https://doi.org/10.1016/J.INTERMET.2016.12.016

Lan, P., Zhang, J., 2017. Twinning and dynamic strain aging behavior during tensile deformation of Fe-Mn-C TWIP steel. Mater. Sci. Eng. A 700, 250–258. https://doi.org/10.1016/j.msea.2017.06.012

Langer, J.S., Bouchbinder, E., Lookman, T., 2010. Thermodynamic theory of dislocation-mediated plasticity. Acta Mater. 58, 3718–3732. https://doi.org/10.1016/j.actamat.2010.03.009

Le, K.C., 2018. Thermodynamic dislocation theory for non-uniform plastic deformations. J. Mech. Phys. Solids 111, 157–169. https://doi.org/10.1016/j.jmps.2017.10.022

Le, K.C., Tran, T.M., Langer, J.S., 2017. Thermodynamic dislocation theory of high-temperature deformation in aluminum and steel. Phys. Rev. E 96, 013004. https://doi.org/10.1103/PhysRevE.96.013004

Li, T.Q., Liu, Y.B., Cao, Z.Y., Wu, R.Z., Zhang, M.L., Cheng, L.R., Jiang, D.M., 2011. The twin mechanism of Portevin Le Chatelier in Mg–5Li–3Al–1.5Zn–2RE alloy. J. Alloys Compd. 509, 7607–7610. https://doi.org/10.1016/j.jallcom.2011.04.099

Ma, A., Roters, F., Raabe, D., 2006. A dislocation density based constitutive model for crystal plasticity FEM including geometrically necessary dislocations. Acta Mater. 54, 2169–2179. https://doi.org/10.1016/j.actamat.2006.01.005

McCormigk, P.G., 1972. A model for the Portevin-Le Chatelier effect in substitutional alloys. Acta Metall. 20, 351–354. https://doi.org/10.1016/0001-6160(72)90028-4

Mecking, H., Kocks, U.F., 1981. Kinetics of flow and strain-hardening. Acta Metall. 29, 1865–1875. https://doi.org/10.1016/0001-6160(81)90112-7

Mughrabi, H., 2016. The α-factor in the Taylor flow-stress law in monotonic, cyclic and quasi-stationary deformations: Dependence on slip mode, dislocation arrangement and density. Curr. Opin. Solid State Mater. Sci. 20, 411–420. https://doi.org/10.1016/J.COSSMS.2016.07.001

Ozgowicz, W., Grzegorczyk, B., 2008. Analysis of the Portevin - Le Chatelier effect in tin bronzes at elevated temperatures. J. Achiev. Mater. Manuf. Eng. 31, 281–289.

Picu, R.C., Vincze, G., Ozturk, F., Gracio, J.J., Barlat, F., Maniatty, A.M., 2005. Strain rate sensitivity of the commercial aluminum alloy AA5182-O. Mater. Sci. Eng. A 390, 334–343. https://doi.org/10.1016/j.msea.2004.08.029

Reed, R.C., 2006. The Superalloys: Fundamentals and Applications. Cambridge University Press, Cambridge. https://doi.org/10.1017/CBO9780511541285

Robinson, J.M., 1994. Serrated flow in aluminium base alloys. Int. Mater. Rev. 39, 217–227. https://doi.org/10.1179/imr.1994.39.6.217

Rodriguez, P., 1984. Serrated plastic flow. Bull. Mater. Sci. 6, 653–663. https://doi.org/10.1007/BF02743993

Shankar, V., Kumar, A., Mariappan, K., Sandhya, R., Laha, K., Bhaduri, A.K., Narasaiah, N., 2017. Occurrence of dynamic strain aging in Alloy 617M under low cycle fatigue loading. Int. J. Fatigue 100, 12–20. https://doi.org/10.1016/j.ijfatigue.2017.03.001

Shannon, C.E., 1948. A Mathematical Theory of Communication. Bell Syst. Tech. J. 27, 379–423. https://doi.org/10.1002/j.1538-7305.1948.tb01338.x

Sleeswyk, A.W., 1958. Slow strain-hardening of ingot iron. Acta Metall. 6, 598–603. https://doi.org/10.1016/0001-6160(58)90101-9

Taylor, G.I., 1934. The Mechanism of Plastic Deformation of Crystals. Part I. Theoretical. Proc. R. Soc. A Math. Phys. Eng. Sci. 145, 362–387. https://doi.org/10.1098/rspa.1934.0106

Truszkowska, A., Yu, Q., Greaney, P.A., Evans, T.M., Kruzic, J.J., 2017. Developing a Crystal Plasticity Model for Metallic Materials Based on the Discrete Element Method. MRS Adv. 1–6. https://doi.org/10.1557/adv.2017.430

Tsai, C.-W., Lee, C., Lin, P.-T., Xie, X., Chen, S., Carroll, R., LeBlanc, M., Brinkman, B.A.W., Liaw, P.K., Dahmen, K.A., Yeh, J.-W., 2019. Portevin-Le Chatelier mechanism in face-centered-cubic metallic alloys from low to high entropy. Int. J. Plast. 122, 212–224. https://doi.org/10.1016/j.ijplas.2019.07.003

Vandermeulen, W., Puzzolante, J.-L., Scibetta, M., 2017. Understanding of Tensile Test Results on Small Size Specimens of Certified Reference Material BCR-661. J. Test. Eval. 45, 20150377. https://doi.org/10.1520/JTE20150377

Wang, W.H., Wu, D., Shah, S.S., Ni, J.H., Chen, R.S., Zhang, X.N., 2017. The relationship between dynamic strain aging and serrated flow behaviour in magnesium alloy. Philos. Mag. Lett. 1–6. https://doi.org/10.1080/09500839.2017.1322723

Ward, E.D., Tallis, W.G., 1956. Tension and Torsion Tests on Nimonic Alloys at High

Temperatures, in: Symposium on Metallic Materials for Service at Temperatures Above 1600 F. ASTM International, 100 Barr Harbor Drive, PO Box C700, West Conshohocken, PA 19428-2959, pp. 135-135–11. https://doi.org/10.1520/STP44993S

Yilmaz, A., 2011. The Portevin–Le Chatelier effect: a review of experimental findings. Sci. Technol. Adv. Mater. 12, 063001. https://doi.org/10.1088/1468-6996/12/6/063001

Yuzbekova, D., Mogucheva, A., Zhemchuzhnikova, D., Lebedkina, T., Lebyodkin, M., Kaibyshev, R., 2017. Effect of microstructure on continuous propagation of the Portevin–Le Chatelier deformation bands. Int. J. Plast. 96, 210–226. https://doi.org/http://dx.doi.org/10.1016/j.ijplas.2017.05.004

Zhang, J., Jiang, Y., 2005. An experimental study of inhomogeneous cyclic plastic deformation of 1045 steel under multiaxial cyclic loading. Int. J. Plast. 21, 2174–2190. https://doi.org/10.1016/j.ijplas.2005.02.003

Zhang, Y., Liu, J.P., Chen, S.Y., Xie, X., Liaw, P.K., Dahmen, K.A., Qiao, J.W., Wang, Y.L., 2017. Serration and noise behaviors in materials. Prog. Mater. Sci. 90, 358–460. https://doi.org/10.1016/j.pmatsci.2017.06.004

Zhu, S.M., Nie, J.F., 2004. Serrated flow and tensile properties of a Mg–Y–Nd alloy. Scr. Mater. 50, 51–55. https://doi.org/10.1016/j.scriptamat.2003.09.039

**Critical velocity of mobile dislocations**

Nimonic 75 at 600 °C

- ● Critical Strain
- ▲ Transformation Strain

Strain rate labels: $1.43 \times 10^{-2}$ /s, $1.43 \times 10^{-3}$ /s, $1.45 \times 10^{-4}$ /s, $1.70 \times 10^{-5}$ /s

$$(\bar{v}_m)_{cr} \approx 1.2 \times 10^{-6} \sim 2.2 \times 10^{-6} \text{ m/s}$$

Type A+B, Type B, Type C+B, Type C & C+B, Type C, Type C+B

Y-axis: Average Velocity of Mobile Dislocation, m/s

X-axis: $\varepsilon_p$, True Plastic Strain

**Model of solute rearrangement across dislocation cores**

$b$

Pinning driven DSA

De-pinning driven DSA

Cr   Ni